Research Square

Preprints are preliminary reports that have not undergone peer review.
They should not be considered conclusive, used to inform clinical practice,
or referenced by the media as validated information.

Parity-Resolved Many-Body Kinetics of a Topological Qubit under Nonequilibrium Phonon Pulses

Han Huang

hh697@cornell.edu

Cornell University

Article

Keywords:

Posted Date: November 25th, 2026

DOI: https://doi.org/10.21203/rs.3.rs-11545246/v1

License: This work is licensed under a Creative Commons Attribution 4.0 International License.
Read Full License

Additional Declarations: No competing interests reported.

Parity-Resolved Many-Body Kinetics of a Topological Qubit under Nonequilibrium Phonon Pulses

Han Huang[1, *]

[1] *Sibley School of Mechanical and Aerospace Engineering, Cornell University, Ithaca, New York 14853, USA*

(Dated: October 29, 2026)

Phonon bursts from ionizing radiation cause correlated errors in superconducting quantum processors. We study prescribed nonequilibrium phonon pulses in a Majorana qubit formed by two 2 μm semiconductor nanowires proximity-coupled to a parent superconductor. We combine the lattice Lutchyn–Oreg model, microscopic electron–phonon coupling, and parity-resolved many-body dynamics to track excitation, relaxation, and logical coherence. Without quasiparticle escape, recombination restores the initial Majorana occupations in about 130 ns. Phonons exchanged during excitation and recovery can nevertheless retain information from the logical state, leaving permanent coherence loss. For mirror-symmetric wires, the fractional coherence loss per wire is 0.75–1.0 times the excitation probability averaged over the two logical states, even at zero Majorana splitting; breaking mirror symmetry can suppress dephasing at small splitting. Factorized Boltzmann kinetics neglects quasiparticle correlations and overestimates residual parity flips. At equal deposited energy density, phonon spectra yield different excitation probabilities and coherence losses. Comparisons with Kitaev chains matched to the wire's gap and Majorana decay length reveal that low electron density suppresses excitation by energetic phonons, whereas hard-wall boundaries in a high-density control increase excitation efficiency by a factor of 5×10^4 relative to the wire for pulses centered at 1 meV. Magnetic-field and chemical-potential tuning yield different phonon sensitivities at the same bulk gap through changes in spin and electron–hole structure. Including hybrid states' semiconductor weights reduces near-threshold excitation rates fourfold when the tunnel coupling equals the parent superconducting gap. Our framework connects phonon spectra to leakage, poisoning, and coherence loss to guide Majorana-device design.

I. INTRODUCTION

Topological qubits encode quantum information in the fermion parities of spatially separated Majorana zero modes. In the topological regime, these modes can form at the ends of semiconductor nanowires coupled to a conventional superconductor [1–7]. Quasiparticle exchange with the environment changes a wire's parity and causes poisoning, which topological protection alone does not prevent [8, 9]. Ionizing radiation provides a possible source of quasiparticle excitations by generating nonequilibrium phonons that propagate through the substrate. In conventional superconducting circuits, these phonons can break Cooper pairs and cause correlated errors across multiple qubits [10–13]. They can also excite bulk quasiparticles in proximitized nanowires. Understanding their effect on Majorana qubits requires answering three questions: which phonons excite the wires, whether the Majorana occupations recover after the pulse, and whether the stored quantum superposition survives.

Previous studies address parts of this problem using different descriptions of the electronic states and their environment. Phonon effects in Majorana wires have been studied for thermal baths [14–17], while radiation models for conventional superconducting circuits focus on phonons above the pair-breaking threshold of aluminum [12, 18]. A nonequilibrium burst has a broader spectral structure, and proximitized wires can also absorb phonons below that threshold. Mean-density and distribution-function approaches [9, 13, 19, 20] describe recombination when quasiparticles encounter one another independently [21], but can miss the correlations within the few pairs created by a weak pulse. Reservoir-arrival models instead describe quasiparticles entering a wire and changing its parity [8]. Master equations have been used to track quasiparticle counts in small islands [22], Andreev levels coupled to a thermal continuum [23], and Kitaev chains in thermal baths [24–27], without directly connecting nonequilibrium phonon spectra to correlated, mode-resolved dynamics in semiconductor wires. Coherence has also been studied under excitation [28–30], prescribed error probabilities [31], classical noise [32–34], and thermal baths with model couplings [26, 35]. For a microscopic phonon pulse, however, it remains unanswered how excitation and relaxation jointly affect populations and coherence, including whether exchanged phonons retain information about the logical state [36].

We calculate the response of a four-Majorana qubit formed by two proximitized nanowires to prescribed nonequilibrium phonon pulses. We obtain the discrete quasiparticle states from the lattice Lutchyn–Oreg model [2, 3] and calculate transition rates from microscopic deformation-potential and piezoelectric couplings. These rates resolve the phonon energy, polarization, and propagation direction. A parity-conserving Pauli master equation evolves the joint occupation probabilities of

* hh697@cornell.edu

the retained modes and preserves pair correlations. We compare its predictions with factorized Boltzmann kinetics, which treats quasiparticle occupations as statistically independent. We then evolve the logical coherence using the many-body density matrix to determine whether the stored quantum superposition survives excitation and recombination, including information about the logical state carried away by phonons. To quantify the correction from semiconductor–superconductor hybridization [37], we compare excitation rates calculated with and without the semiconductor weight of hybrid quasiparticle states. To test which results require the semiconductor band structure, we compare the nanowire with spinless Kitaev chains [1] having the same gap and Majorana decay length, at both comparable and higher electron densities.

For 2 μm wires with InAs-like effective parameters, recombination restores the initial Majorana occupations on a mean timescale of about 130 ns when quasiparticles cannot escape. Permanent parity poisoning requires quasiparticle exchange with the environment, whereas factorized Boltzmann kinetics predicts a spurious residual Majorana occupation of roughly twice the excitation probability in the weak-pulse limit. Parity recovery nevertheless leaves a loss of logical coherence because the exchanged phonons can distinguish the logical states. At equal deposited energy density, different pulse spectra produce substantially different excitation probabilities and coherence losses. The electronic structure further controls this response: at low electron density, momentum mismatch suppresses excitation by high-energy phonons. At zero chemical potential, a selection rule also weakens the coupling of phonons to the low-energy states near the field-driven transition. Consequently, reducing the gap by tuning the magnetic field does not strongly enhance phonon excitation. These results show why neither the excitation gap nor parity recovery alone determines resilience to phonon bursts. Our framework connects nonequilibrium phonon spectra to quasiparticle dynamics and logical coherence, providing a microscopic basis for assessing radiation sensitivity in Majorana qubits. By resolving how electronic structure and device symmetry influence excitation and coherence loss, it can guide the choice of device geometries and operating conditions that reduce susceptibility to phonon bursts.

II. MODEL

A. Qubit and wire spectrum

We consider two identical parallel wires separated by $d = 300$ nm, with no tunneling between them [Fig. 1(a)]. Wire 1 hosts the Majorana end modes γ_1 and γ_2, and wire 2 hosts γ_3 and γ_4. The two Majorana modes in each wire form one fermionic mode with occupation $n_0 = 0$ or 1. We use the even-total-parity states

$$|0_L\rangle = |00\rangle, \qquad |1_L\rangle = |11\rangle \tag{1}$$

as the logical basis, with all bulk quasiparticle modes empty. Here the two entries specify the fermionic occupations in wires 1 and 2. The operators X_L, Y_L, and Z_L are the Pauli operators in this basis. The off-diagonal density-matrix element $\rho_{01} = \langle 0_L|\rho|1_L\rangle$ measures the logical coherence. Bulk quasiparticles in either wire cause leakage from the logical subspace. Quasiparticle exchange with an external reservoir can leave a wire's Majorana occupation flipped after the bulk empties. This residual flip is poisoning.

Each wire is described by the Lutchyn–Oreg model [2, 3], which combines a semiconductor band, Rashba spin–orbit coupling α, a Zeeman energy V_Z along the wire, and a fixed induced pairing Δ. We introduce the four-component Nambu field operator

$$\Psi = (\psi_\uparrow, \psi_\downarrow, \psi_\downarrow^\dagger, -\psi_\uparrow^\dagger)^T, \tag{2}$$

where $\psi_\sigma(x)$ annihilates an electron with spin σ at position x, and $\psi_\sigma^\dagger(x)$ creates one. In this time-reversed-hole basis, the Hamiltonian is

$$H_{\rm LO} = \left(-\frac{\hbar^2\partial_x^2}{2m^*} - \mu\right)\tau_z - i\alpha\partial_x\sigma_y\tau_z + V_Z\sigma_x + \Delta\tau_x, \tag{3}$$

where m^* is the effective mass, μ is the chemical potential, and σ_i and τ_i are Pauli matrices acting in spin and particle–hole space, respectively.

We discretize the wire with lattice spacing a and define $t_0 = \hbar^2/(2m^*a^2)$. The on-site and nearest-neighbor blocks are

$$\begin{aligned} H_{ii} &= (2t_0 - \mu)\tau_z + V_Z\sigma_x + \Delta\tau_x, \\ H_{i,i+1} &= -t_0\tau_z - \frac{i\alpha}{2a}\sigma_y\tau_z. \end{aligned} \tag{4}$$

There are $L/a - 1$ interior sites, with hard-wall boundaries at $x = 0$ and $x = L$. In this representation H is real, and particle–hole conjugation is $\mathcal{C} = \tau_y\sigma_y K$, where K denotes complex conjugation.

The lattice topological invariant is

$$\begin{aligned} \mathcal{Q} = \mathrm{sgn}\big[&(\mu^2 + \Delta^2 - V_Z^2) \\ &\times \big((4t_0 - \mu)^2 + \Delta^2 - V_Z^2\big)\big]. \end{aligned} \tag{5}$$

The topological phase has $\mathcal{Q} = -1$. At the low fillings considered here ($|\mu|, \Delta, V_Z \ll 4t_0$), this condition reduces to $V_Z > \sqrt{\mu^2 + \Delta^2}$.

Diagonalizing the finite-wire Hamiltonian gives the positive-energy modes Φ_a and energies E_a. The lowest mode, Φ_0, has energy $E_0 \equiv \epsilon_M \geq 0$ and is formed from the two end-localized, self-conjugate spinors Φ_L and Φ_R, for which $\mathcal{C}\Phi_{L,R} = \Phi_{L,R}$. Their overlap produces the finite splitting ϵ_M. We refer to the modes $a > 0$ as bulk modes and retain all positive-energy modes below 1.2 meV.

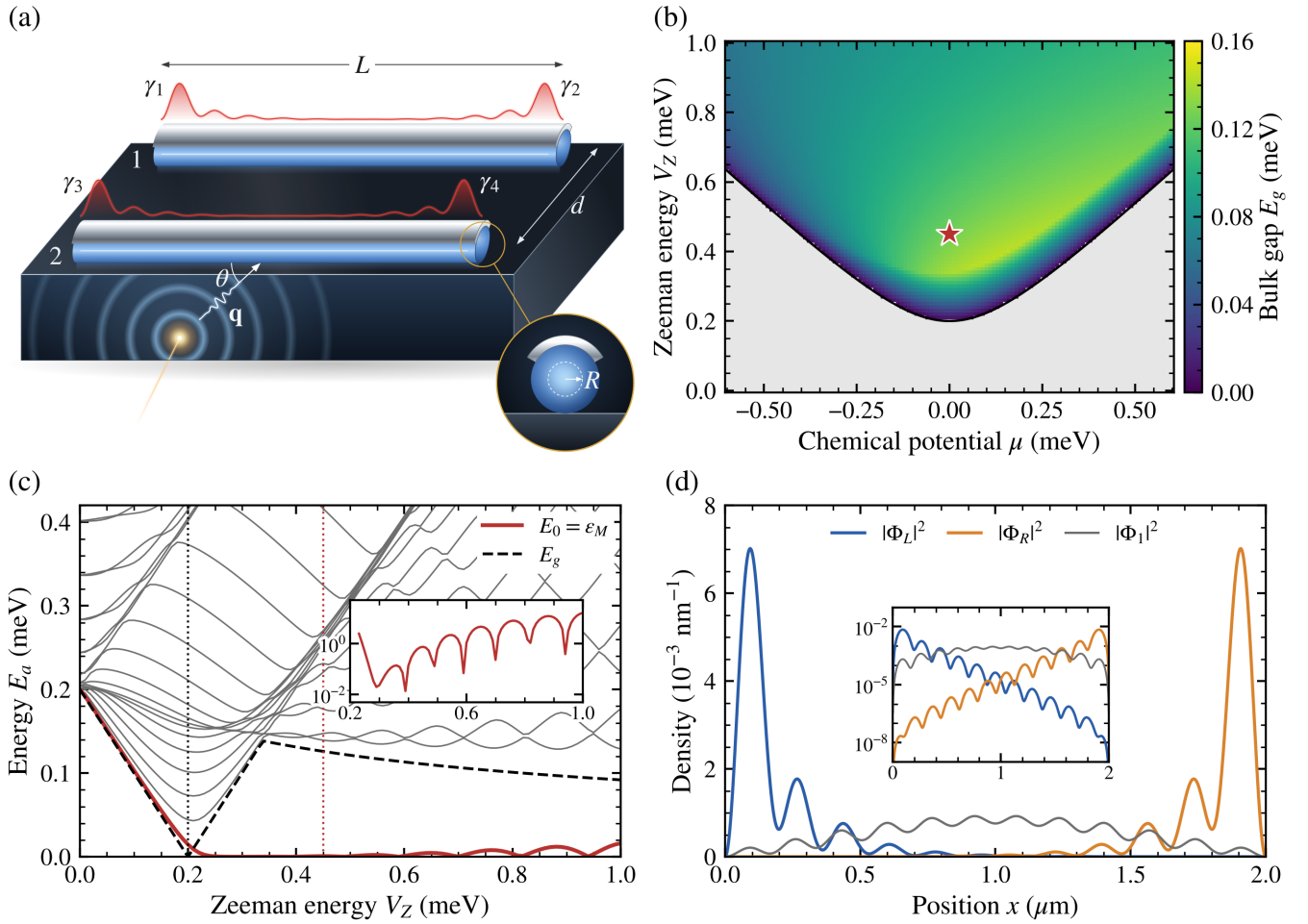

FIG. 1. Qubit geometry and wire spectrum. (a) Two parallel semiconductor wires (blue), each coupled to a superconducting shell (gray), host four Majorana end modes $\gamma_1, \ldots, \gamma_4$. The wires have length L and separation d. A phonon generated by a radiation impact in the substrate reaches a wire at angle θ to its axis. (b) Bulk gap E_g of the infinite lattice wire in the topological phase, $\mathcal{Q} = -1$. Gray marks the trivial phase, the black line is $V_Z = \sqrt{\mu^2 + \Delta^2}$, and the star marks the working point. (c) Positive eigenenergies of the finite 2 μm wire versus V_Z at $\mu = 0$. Gray lines show the excited modes, red shows the lowest energy $E_0 = \epsilon_M$, and the dashed line shows the bulk gap. Vertical dotted lines mark $V_Z = \Delta$ and the working point. The inset shows ϵ_M in μeV on a logarithmic scale. (d) Spatial densities of the Majorana spinors Φ_L and Φ_R and the lowest bulk mode Φ_1 at the working point. The inset shows the same densities in nm^{-1} on a logarithmic scale versus x in μm.

We use InAs-like effective parameters: $m^* = 0.023\, m_e$, $\alpha = 20$ meV nm, $\mu = 0$, $V_Z = 0.45$ meV, and $\Delta = 0.20$ meV. Each wire is 2 μm long and is discretized with spacing $a = 2.5$ nm. The phonon bath is at 20 mK, and the pulse has a Gaussian time envelope with a full width at half maximum of 50 ns. These values define the reference working point. Appendix A lists the remaining material inputs, pulse spectra, and numerical settings.

B. Electron-phonon coupling

A phonon mode λ produces a local potential $g_\lambda(x)$ in the semiconductor. Because this potential modifies electron and hole energies with opposite signs, it adds the perturbation $V_\lambda = g_\lambda(x)\tau_z$ to $H_{\rm LO}$. In the quasiparticle basis of $H_{\rm LO}$, this perturbation gives the coupling operator

$$O_\lambda = \sum_{ab} A^\lambda_{ab} c^\dagger_a c_b + \sum_{a<b} \left(B^\lambda_{ab} c^\dagger_a c^\dagger_b + \text{h.c.} \right), \qquad (6)$$

with matrix elements

$$\begin{aligned} A^\lambda_{ab} &= \langle \Phi_a | V_\lambda | \Phi_b \rangle, \\ B^\lambda_{ab} &= \langle \Phi_a | V_\lambda \mathcal{C} | \Phi_b \rangle. \end{aligned} \qquad (7)$$

The off-diagonal A terms describe phonon-mediated quasiparticle transitions from mode b to mode a. The diagonal terms shift the energy of an occupied mode. The B terms create or annihilate a pair. For real standing-wave phonons, $A = A^\dagger$ and $B = -B^T$, so $B_{aa} = 0$: a pair cannot occupy the same quasiparticle mode. For

the incoherent, isotropic phonon bath considered here, real standing-wave modes and traveling-wave modes give identical total transition rates. We can therefore use either representation.

We model phonons as plane waves in an isotropic elastic continuum. Longitudinal acoustic (LA) phonons couple through the deformation potential, with amplitude iDq, where D is the deformation-potential constant and $q = |\mathbf{q}|$. In zincblende InAs, both LA and transverse acoustic (TA) phonons also produce a piezoelectric potential. Its amplitude is $P\,\mathbf{f}(\hat{\mathbf{q}})\cdot\mathbf{e}$, where

$$\begin{aligned}\mathbf{f} &= (\hat{q}_y\hat{q}_z, \hat{q}_z\hat{q}_x, \hat{q}_x\hat{q}_y),\\ P &= \frac{2ee_{14}}{\varepsilon_0\varepsilon_r} = 671\ \mathrm{meV\,nm^{-1}}.\end{aligned} \tag{8}$$

Here $\mathbf{e}$ is the polarization vector, the components of $\hat{\mathbf{q}}$ are expressed in crystal axes, e is the positive elementary charge, and e_{14} is the piezoelectric coefficient.

The transverse electron density is Gaussian with $1/e$ radius R. Its form factor is

$$|F_\perp(q_\perp)|^2 = e^{-q_\perp^2 R^2/2}, \tag{9}$$

which suppresses coupling to phonons with transverse wave vector much larger than $1/R$.

To calculate transition rates from the matrix elements A_{ab} and B_{ab}, we separate the electronic spatial overlap from the phonon coupling factors. For a phonon whose wave-vector component along the wire is k, the electronic factor is

$$M_{ab}(k) = \sum_i e^{ikx_i}\rho_{ab}(x_i), \tag{10}$$

where

$$\rho_{ab}(x_i) = \begin{cases}\Phi_a^\dagger(x_i)\tau_z\Phi_b(x_i), & \text{scattering},\\ \Phi_a^\dagger(x_i)\tau_z\mathcal{C}\Phi_b(x_i), & \text{pair creation}.\end{cases} \tag{11}$$

M_{ab} is the electronic part of the corresponding A_{ab} or B_{ab} matrix element. It determines the coupling between the two quasiparticle modes for a phonon with a given longitudinal wave vector.

Fermi's golden rule, integrated over phonon propagation directions, gives the transition rate per unit phonon occupation:

$$\gamma_{ab}^\nu(\Omega) = \frac{q}{8\pi^2\hbar\rho c_\nu^2}\int_{-1}^{1} d\cos\theta\,\bar{C}_\nu(\theta,q) \times |F_\perp(q\sin\theta)|^2|M_{ab}(q\cos\theta)|^2, \tag{12}$$

where $\Omega > 0$ is the energy exchanged with the phonon, ρ is the material mass density, and c_ν is the sound velocity of branch ν. Energy conservation fixes $q = \Omega/(\hbar c_\nu)$, and θ is the angle between the phonon wave vector and the wire axis. The factors $F_\perp(q\sin\theta)$ and $M_{ab}(q\cos\theta)$ account for the transverse and longitudinal spatial overlaps, respectively.

To obtain $\bar{C}_\nu$, we add the coupling amplitudes for each phonon mode and take their squared magnitude. We then integrate over the azimuthal angle ϕ:

$$\bar{C}_\nu(\theta,q) = \int_0^{2\pi} d\phi \sum_{s=1}^{g_\nu} \times \left|iDq\,\delta_{\nu,\mathrm{LA}} + P\,\mathbf{f}(\hat{\mathbf{q}})\cdot\mathbf{e}_{\nu s}\right|^2. \tag{13}$$

Here s labels the polarization, with $g_{\mathrm{LA}} = 1$ and $g_{\mathrm{TA}} = 2$, and $\delta_{\nu,\mathrm{LA}}$ restricts deformation-potential coupling to LA phonons. The phonon direction and polarization are expressed in crystal axes when evaluating $\mathbf{f}\cdot\mathbf{e}_{\nu s}$.

For an LA phonon, both mechanisms contribute to the same mode. With real polarization vectors, the deformation-potential amplitude iDq is purely imaginary, whereas the piezoelectric amplitude $P\,\mathbf{f}\cdot\mathbf{e}_{\mathrm{LA}}$ is real. Their interference term, $2\,\mathrm{Re}[(iDq)(P\,\mathbf{f}\cdot\mathbf{e}_{\mathrm{LA}})^*]$, therefore vanishes. The squared total amplitude therefore separates into deformation-potential and piezoelectric contributions:

$$\bar{C}_{\mathrm{LA}}^{\mathrm{DP}} = 2\pi D^2 q^2, \tag{14}$$

and

$$\bar{C}_\nu^{\mathrm{PE}} = P^2\int_0^{2\pi} d\phi \sum_{s=1}^{g_\nu} \left|\mathbf{f}(\hat{\mathbf{q}})\cdot\mathbf{e}_{\nu s}\right|^2. \tag{15}$$

Thus, $\bar{C}_{\mathrm{LA}} = \bar{C}_{\mathrm{LA}}^{\mathrm{DP}} + \bar{C}_{\mathrm{LA}}^{\mathrm{PE}}$, while $\bar{C}_{\mathrm{TA}} = \bar{C}_{\mathrm{TA}}^{\mathrm{PE}}$.

γ_{ab}^ν contains the microscopic coupling strength and is independent of the phonon occupation. Multiplying it by $N_\nu(\Omega,t)$ gives the absorption rate, while multiplying it by $N_\nu(\Omega,t)+1$ gives the emission rate. After summing over branches, these rates enter the Pauli master equation for the quasiparticle occupation configurations. The same γ_{ab}^ν values provide the transition-line weights in the excitation kernel defined below.

C. Excitation kernel and pulses

When the bulk is empty, a phonon can excite the wire through three channels. If the Majorana occupation is $p = n_0 = 0$, it can create a pair consisting of one excitation in the Majorana fermionic mode and one in bulk mode a. This process has weight $|B_{0a}|^2$ and requires energy $E_a+\epsilon_M$. If $p = 1$, it can instead promote the existing quasiparticle into bulk mode a, with weight $|A_{a0}|^2$ and energy $E_a - \epsilon_M$. For either value of p, it can also create two bulk quasiparticles, with weight $|B_{ab}|^2$ and energy $E_a + E_b$, where $0 < a < b$.

We collect these discrete transitions into the excitation kernel

$$\mathcal{K}_\nu^{(p)}(\Omega) = \sum_\ell \gamma_\ell^\nu\,\delta(\Omega - \Omega_\ell), \tag{16}$$

where ℓ labels an individual allowed excitation for the specified initial Majorana occupation p. This kernel gives

the excitation rate per unit phonon occupation and unit phonon energy. For an isotropic occupation $N_\nu(\Omega,t)$, the total rate is

$$\Gamma^{(p)}_{\rm exc}(t)=\sum_\nu\int d\Omega\,\mathcal{K}^{(p)}_\nu(\Omega)N_\nu(\Omega,t). \tag{17}$$

For plotting, we broaden each line with a Gaussian of the width specified in Appendix A.

A pulse adds the excess occupation

$$\delta N(\Omega,t)=\mathcal{A}\,s(t)\,\pi(\Omega) \tag{18}$$

to the 20-mK bath. We use the same excess occupation for all phonon branches. The envelope $s(t)$ sets the time dependence, while $\pi(\Omega)$ sets the spectrum. We consider a narrowband Gaussian centered at Ω_c, a broadband step, and a thermal excess $n_B(\Omega,T^*)-n_B(\Omega,T_{\rm bath})$ for comparison.

The amplitude $\mathcal{A}$ fixes the peak excess phonon energy density,

$$\begin{aligned} u&=\sum_\nu\int d\Omega\,\frac{F_\nu}{V}\,\Omega\,\delta N_\nu(\Omega),\\ \frac{F_\nu}{V}&=\frac{g_\nu\Omega^2}{2\pi^2\hbar^3c_\nu^3}, \end{aligned} \tag{19}$$

where F_ν/V is the phonon density of states per unit volume, with $g_{\rm LA}=1$ and $g_{\rm TA}=2$. Here $\delta N_\nu(\Omega)$ denotes the occupation at the pulse peak. We compare pulses with different spectra at the same peak excess energy density u and temporal envelope $s(t)$ to isolate the spectrum's effect on excitation probabilities and logical coherence loss. Their weak-pulse excitation efficiencies are

$$\eta=\lim_{u\to0}\frac{P_{\rm exc}}{u}, \tag{20}$$

Here $P_{\rm exc}\equiv P^{(0)}_{\rm exc}$ is the probability of at least one excitation during the pulse, starting with an empty Majorana level and no bulk quasiparticles [Eq. (28)]. Thus η measures excitation probability per unit excess energy density in the weak-pulse limit.

D. Parity-resolved kinetics

A weak pulse creates only a few quasiparticles, and their occupations can remain correlated. We therefore evolve the probability P_n of each many-body configuration

$$|n\rangle=\prod_a(c_a^\dagger)^{n_a}|{\rm vac}\rangle,\qquad n_a=0,1, \tag{21}$$

using the configuration-resolved Pauli master equation. For $\Omega_{ab}=|E_a-E_b|>0$, the single-process scattering rate is

$$W_{a\leftarrow b}(t)=\sum_\nu\gamma^{\nu,A}_{ab}(\Omega_{ab})\begin{cases}N_\nu(\Omega_{ab},t), & E_a>E_b,\\ N_\nu(\Omega_{ab},t)+1, & E_a<E_b.\end{cases} \tag{22}$$

Pair creation and recombination have rates

$$\begin{aligned} W^+_{ab}(t)&=\sum_\nu\gamma^{\nu,B}_{ab}(E_a+E_b)N_\nu(E_a+E_b,t),\\ W^-_{ab}(t)&=\sum_\nu\gamma^{\nu,B}_{ab}(E_a+E_b)[N_\nu(E_a+E_b,t)+1]. \end{aligned} \tag{23}$$

The superscripts A and B specify the scattering or pair-creation form factor in Eq. (12). All W have units of inverse time and exclude electronic occupation factors.

Let $R_{m\leftarrow n}$ denote the rate from configuration n to m, and let $\mathbf{e}_a$ change occupation n_a by one. The nonzero phonon-induced rates are

$$\begin{aligned} R_{n+\mathbf{e}_a-\mathbf{e}_b\leftarrow n}&=W_{a\leftarrow b}n_b(1-n_a), && a\neq b,\\ R_{n+\mathbf{e}_a+\mathbf{e}_b\leftarrow n}&=W^+_{ab}(1-n_a)(1-n_b), && a<b,\\ R_{n-\mathbf{e}_a-\mathbf{e}_b\leftarrow n}&=W^-_{ab}n_an_b, && a<b. \end{aligned} \tag{24}$$

The occupation factors restrict transitions to valid fermionic configurations. The configuration probabilities obey

$$\dot P_n(t)=\sum_{m\neq n}\left[R_{n\leftarrow m}(t)P_m(t)-R_{m\leftarrow n}(t)P_n(t)\right]. \tag{25}$$

Equivalently, $\dot{\mathbf{P}}=\mathcal{L}(t)\mathbf{P}$, with

$$\mathcal{L}_{nm}=\begin{cases}R_{n\leftarrow m}, & n\neq m,\\ -\sum_{k\neq n}R_{k\leftarrow n}, & n=m.\end{cases} \tag{26}$$

Every phonon-induced jump changes the quasiparticle number by zero or two. Thus $R_{m\leftarrow n}=0$ between configurations of opposite parity, $\pi_n=(-1)^{\sum_a n_a}$, and Eq. (25) evolves the even and odd sectors separately. An initially empty bulk with Majorana occupation p starts in the sector $\pi=(-1)^p$.

The logical subspace is spanned by $|0_L\rangle=|00\rangle$ and $|1_L\rangle=|11\rangle$, where the two entries denote the Majorana-level occupations of the two wires and all bulk quasiparticle modes are empty. A bulk excitation in either wire takes the qubit outside this subspace.

For each wire, we retain configurations with at most $k_{\rm max}$ bulk quasiparticles. We separately monitor the probability flowing beyond this cutoff to assess numerical truncation error. Within the retained space, the joint configuration probabilities preserve correlations between all mode occupations.

We monitor the bulk leakage probability, which measures whether any bulk mode is occupied, and the probability that the Majorana occupation differs from its initial value:

$$\begin{aligned} P_{\rm leak}&=1-\sum_n\prod_{a>0}(1-n_a)P_n,\\ P_{\rm flip}&=\sum_{n:\,n_0\neq p}P_n, \end{aligned} \tag{27}$$

where p is the initial Majorana occupation. The Majorana occupation change described by $P_{\rm flip}$ can occur transiently while the total wire parity remains unchanged.

Starting with an empty bulk and Majorana occupation p, we calculate the probability that the pulse produces at least one bulk excitation, whether or not the bulk later returns to its empty state:

$$P_{\rm exc}^{(p)} = 1 - \exp\left[-\int dt\, \Gamma_{\rm exc}^{(p)}(t)\right]. \tag{28}$$

We write $P_{\rm exc}$ for the case $p = 0$. We characterize recovery by the mean time required for the bulk to empty,

$$\tau_{\rm return} = -\mathbf{1}^T \mathcal{L}_b^{-1} \mathbf{P}_*. \tag{29}$$

Here $\mathcal{L}_b$ contains only the equilibrium-bath transitions and is restricted to configurations with a nonempty bulk. We evaluate the post-pulse distribution $\mathbf{P}_*$ at $t_* = t_c + 6\sigma_t$, where t_c is the pulse-center time and σ_t is the temporal standard deviation of the Gaussian envelope. By this time, the pulse has effectively ended. We include only configurations that still contain bulk quasiparticles and normalize their probabilities to sum to one. An excitation followed by a return to the empty bulk forms a complete excursion out of the code space.

For comparison, we solve the factorized Boltzmann equation using the same transition-rate tables. This approximation replaces joint occupation averages by products, $\langle n_a n_b\rangle = f_a f_b$, where $f_a = \langle n_a\rangle$. It gives

$$\begin{aligned}\dot{f}_a = &\sum_{b\neq a} \left[W_{a\leftarrow b} f_b(1-f_a) - W_{b\leftarrow a} f_a(1-f_b)\right] \\ &+ \sum_{b\neq a} \left[W_{ab}^{+}(1-f_a)(1-f_b) - W_{ab}^{-} f_a f_b\right]. \end{aligned} \tag{30}$$

The two calculations use identical microscopic rates, so differences between them isolate the effect of neglecting occupation correlations.

We also allow bulk quasiparticles to escape to an external reservoir at a phenomenological rate $\Gamma_{\rm esc}$. In $\mathcal{L}$, each escape jump empties an occupied bulk mode. In Eq. (30), it adds $-\Gamma_{\rm esc} f_a$ for $a > 0$. Each escape event changes the parity of the wire. Its contribution to Eq. (25) is

$$R^{\rm esc}_{n-\mathbf{e}_a\leftarrow n} = \Gamma_{\rm esc} n_a, \qquad a > 0, \tag{31}$$

which couples the even- and odd-parity sectors.

E. Logical coherence

Excitation can transfer coherence outside the code space, and relaxation can return it when the bulk empties. To distinguish this temporary transfer from irreversible coherence loss, we supplement the population dynamics with selected off-diagonal elements of the many-body density matrix, evolved under a Born–Markov master equation with the same coupling vertices [38].

We label configurations by $|n_0, S\rangle$, where n_0 is the Majorana occupation and S lists the occupied bulk modes; the partner wire's Majorana occupation is implicit in these labels. We define

$$\chi_S(t) = \frac{\langle 0, S|\rho(t)|1, S\rangle}{\langle 0, \varnothing|\rho(0)|1, \varnothing\rangle}. \tag{32}$$

For each fixed configuration S, $\chi_S(t)$ tracks the coherence between the two Majorana occupations, normalized to the initial empty-bulk coherence. The quantity $\chi_\varnothing$ measures coherence in the empty-bulk sector. Transitions involving bulk modes alone leave n_0 unchanged and act identically on the two branches. They transfer coherence from χ_S to $\chi_{S'}$ at the same rate as the corresponding population transition. Subsequent processes involving the Majorana level can allow phonons to distinguish the branches and destroy this coherence. Tracking the χ_S determines how much coherence returns to the empty-bulk sector and how much is lost during the excursion.

We evolve one wire while treating the other as a spectator. The partner wire's Majorana occupation remains an implicit label of the two logical branches, so these matrix elements retain the two-wire logical coherence. Escape acts only on the active wire, but can change the total parity of the two-wire system. We therefore retain the partner wire's Majorana occupation as an independent state label instead of inferring it from the fixed-parity constraint.

Transitions that change n_0 can distinguish the logical branches: pair creation exchanges a phonon of energy $E_a + \epsilon_M$, whereas promotion exchanges one of energy $E_a - \epsilon_M$. These processes interchange the Majorana occupations. They damp coherence at the mean of the branch rates and transfer it between configurations S and $S \pm a$, where $S \pm a$ denotes adding or removing bulk mode a. The matrix-element equations below fix the transfer signs and conjugations explicitly.

To compare the phonon mode profiles of promotion and pair creation, we calculate the promotion rate coefficient Γ_a^A, the pair-creation rate coefficient Γ_a^B, and the coherence-transfer coefficient $\Gamma_a^\times$ at the common energy $\Omega = E_a$, before including phonon occupation factors. The direct coefficients are

$$\Gamma_a^A = \sum_\nu \gamma_{a0}^{\nu,A}(E_a), \qquad \Gamma_a^B = \sum_\nu \gamma_{a0}^{\nu,B}(E_a), \tag{33}$$

where Eq. (12) uses the electronic form factors M_{a0}^A for promotion and M_{a0}^B for pair creation. The cross coefficient contains their amplitude product and governs coherence transfer:

$$\begin{aligned}\Gamma_a^\times = \sum_\nu \frac{q_\nu}{8\pi^2\hbar\rho c_\nu^2} \int_{-1}^{1} d\cos\theta\, \bar{C}_\nu(\theta, q_\nu) |F_\perp(q_\nu \sin\theta)|^2 \\ \times M_{a0}^B(q_\nu\cos\theta) M_{a0}^A(q_\nu\cos\theta)^*, \end{aligned} \tag{34}$$

with $q_\nu = E_a/(\hbar c_\nu)$.

The normalized overlap is

$$\kappa_a = \frac{|\Gamma_a^{\times}|}{\sqrt{\Gamma_a^A \Gamma_a^B}} \leq 1. \tag{35}$$

At this common energy, $\kappa_a = 0$ means that the phonon states are orthogonal and distinguish the branches, while $\kappa_a = 1$ means that their normalized mode profiles are identical up to a phase. For absorption or emission, the corresponding kinetic coefficients are obtained by multiplying each branch contribution to all three coefficients by $N_\nu(E_a, t)$ or $N_\nu(E_a, t) + 1$, respectively. Vanishing κ_a does not imply complete qubit dephasing: the pulse-averaged loss also depends on the probability of taking the corresponding excitation paths (Appendix B).

The explicit coherence equations use the same fermionic transition operators as the population kinetics. For $a > 0$, define the pair-creation and promotion operators

$$F_{aB}^{+} = c_a^\dagger c_0^\dagger, \qquad F_{aA}^{+} = c_a^\dagger c_0, \qquad F_{aX}^{-} = (F_{aX}^{+})^\dagger. \tag{36}$$

The order $c_a^\dagger c_0^\dagger$ matches the vertex B_{a0} in Eq. (34). The absorption and emission blocks, ordered as (B, A), are

$$\begin{aligned} \mathsf{C}_a^{+} &= \begin{pmatrix} d_{aB}^{+} & r_a^{+} \\ (r_a^{+})^* & d_{aA}^{+} \end{pmatrix}, \\ \mathsf{C}_a^{-} &= \begin{pmatrix} d_{aB}^{-} & (r_a^{-})^* \\ r_a^{-} & d_{aA}^{-} \end{pmatrix}, \end{aligned} \tag{37}$$

where

$$\begin{aligned} (d_{aB}^{+}, d_{aA}^{+}) &= (W_{0a}^{+}, W_{a\leftarrow 0}), \\ (d_{aB}^{-}, d_{aA}^{-}) &= (W_{0a}^{-}, W_{0\leftarrow a}). \end{aligned} \tag{38}$$

Writing $\gamma_a^{\nu,\times}$ for the contribution of branch ν to Eq. (34), the common-energy cross coefficients are

$$\begin{aligned} r_a^{+}(t) &= \sum_\nu N_\nu(E_a, t)\gamma_a^{\nu,\times}, \\ r_a^{-}(t) &= \sum_\nu [N_\nu(E_a, t) + 1]\gamma_a^{\nu,\times}. \end{aligned} \tag{39}$$

Reversing the transition operators and their microscopic amplitudes gives the conjugation in the emission block.

Let α label these two-channel blocks and the remaining single-channel jumps. The single-channel jumps are bulk scattering $c_a^\dagger c_b$ with rate $W_{a\leftarrow b}$, bulk-pair creation $c_a^\dagger c_b^\dagger$ and recombination with rates W_{ab}^{+} and W_{ab}^{-}, and escape c_a with rate $\Gamma_{\rm esc}$. The bulk-only indices satisfy $a, b > 0$, with $a \neq b$ for scattering and $a < b$ for pair processes. Each single-channel block has its rate as its sole matrix entry. In a frame removing the spectator wire's known free precession, the master equation is

$$\begin{aligned} \dot\rho = &-\frac{i}{\hbar}[H_{\rm qp}, \rho] \\ &+ \sum_{\alpha,ij} (\mathsf{C}_\alpha)_{ij} \left(F_{\alpha i}\rho F_{\alpha j}^\dagger - \frac{1}{2}\{F_{\alpha j}^\dagger F_{\alpha i}, \rho\} \right), \end{aligned} \tag{40}$$

where $H_{\rm qp} = \sum_a E_a c_a^\dagger c_a$ acts on the active wire, while ρ retains both wires' state labels. The Hamiltonian Lamb shift is omitted.

To write the equations for the retained matrix elements explicitly, let $\rho_{nm} = \langle n|\rho|m\rangle$, with the spectator occupation included in n, m, and define

$$\begin{aligned} K_{nm;kl} = &\sum_{\alpha,ij} (\mathsf{C}_\alpha)_{ij} \\ &\times \langle n|F_{\alpha i}|k\rangle \langle m|F_{\alpha j}|l\rangle^*. \end{aligned} \tag{41}$$

For these transition blocks the loss operator is diagonal in the occupation basis. With $E_n = \sum_a E_a n_a$ and total outgoing rate $\Lambda_n = \sum_{k\neq n} K_{kk;nn}$, the component equation is

$$\begin{aligned} \dot\rho_{nm} = &\left[-\frac{i(E_n - E_m)}{\hbar} - \frac{\Lambda_n + \Lambda_m}{2} \right] \rho_{nm} \\ &+ \sum_{kl} K_{nm;kl}\rho_{kl}. \end{aligned} \tag{42}$$

For populations, $K_{nn;kk} = R_{n\leftarrow k}$, recovering Eq. (25). The off-diagonal equation describes coherence transfer between configurations and damping at the mean outgoing rate. Let n_S and m_S label the two many-body configurations whose coherence is tracked by χ_S. We write each configuration as $(n_0, S; n_{\rm sp})$, where n_0 is the active wire's Majorana occupation, S lists its occupied bulk modes, and $n_{\rm sp}$ is the spectator wire's Majorana occupation. The spectator bulk remains empty.

Without escape, the total parity remains even, so

$$\begin{aligned} &n_S = (0, S; r_S), \qquad m_S = (1, S; 1 - r_S), \\ &r_S = |S| \bmod 2. \end{aligned} \tag{43}$$

Here $|S|$ counts the bulk quasiparticles. Thus $r_S = 0$ for an even number and $r_S = 1$ for an odd number; the spectator occupations shown above ensure even total parity in both configurations. For $C_0 = \rho_{01}(0) \neq 0$, the closed same-bulk-configuration equations are

$$\begin{aligned} \dot\chi_S = &\left[\frac{i\epsilon_M}{\hbar} - \frac{\Lambda_{n_S} + \Lambda_{m_S}}{2} \right] \chi_S \\ &+ \sum_T K_{n_S m_S; n_T m_T}\chi_T \\ &+ \frac{C_0^*}{C_0} \sum_T K_{n_S m_S; m_T n_T}\chi_T^*. \end{aligned} \tag{44}$$

The phase factor is unity for real initial coherence. Keeping it allows an arbitrary initial logical phase. Additional coherences between different bulk configurations are omitted in this closure. With escape, the spectator occupation is independent and Eq. (42) is used with the full state labels. The fermionic matrix elements in Eq. (41) fix all transfer signs, including those associated with escape.

Complete positivity is ensured when each C_α is positive semidefinite. This is guaranteed by a consistent

common-energy construction, but is not implied by the bare overlap bound when the direct rates use $E_a \pm \epsilon_M$ and the cross coefficient uses E_a. Appendix C gives the explicit condition, its proof, and the distinction between these rate conventions.

The Majorana splitting can also suppress coherence transfer. Free evolution rotates χ_S and χ_S^* at opposite frequencies, $\epsilon_M/\hbar$ and $-\epsilon_M/\hbar$. When their frequency difference $2\epsilon_M/\hbar$ is much larger than the transition rates, the transfer terms oscillate rapidly and average out. We therefore neglect these coherence-transfer terms in this regime.

The generator is constant after the pulse. We obtain the final coherence, $\chi = \chi_{\varnothing}(\infty)$, by solving one linear system in a frame that removes the free precession. Without escape, and after the bulk has emptied, the pulse acts on the logical state as $\rho_{01} \to \chi\rho_{01}$, a channel diagonal in Z_L. For independent events in the two wires, their coherence factors multiply.

The splitting scans in Sec. III D vary ϵ_M while keeping the wave functions fixed. For transitions involving the Majorana mode, the vertices are evaluated at $\Omega = E_a$, and the final coherence is calculated to first order in the phonon energy density u.

F. Parent superconductor

The fixed-pairing model places the entire quasiparticle state in the semiconductor. In a hybrid device, each state has weight in both the semiconductor and the superconducting shell. The phonon potential considered here acts in the semiconductor, so the excitation matrix elements depend on how much of each state lies there.

To quantify this correction, we compare the fixed-pairing description with a bare wire h_w that has $\Delta = 0$ and is tunnel coupled to a parent superconductor. The parent has gap Δ_S and an energy-independent normal-state density of states. Integrating out the parent gives

$$\Sigma_S(E) = -\gamma_t \frac{E\tau_0 - \Delta_S\tau_x}{\sqrt{\Delta_S^2 - E^2}}, \tag{45}$$

where γ_t sets the tunneling strength.

The bound-state energies below the parent gap satisfy

$$[E_a - h_w - \Sigma_S(E_a)]\varphi_a = 0. \tag{46}$$

We choose $\varphi_a^\dagger\varphi_a = 1$. Normalization of the full hybrid state then gives the semiconductor weight Z_a through [37]

$$Z_a^{-1} = \varphi_a^\dagger[1 - \partial_E\Sigma_S(E_a)]\varphi_a. \tag{47}$$

The semiconductor component of the normalized hybrid state is $w_a = \sqrt{Z_a}\,\varphi_a$. A perturbation δh_w acting in the semiconductor therefore has the matrix element

$$A_{ab} = \sqrt{Z_a Z_b}\,\varphi_a^\dagger \delta h_w \varphi_b. \tag{48}$$

Each transition thus depends on the semiconductor components of both states. We solve for the poles below $0.97\Delta_S$, where the semiconductor weight is already small. Higher-energy bound states approach Δ_S, and their semiconductor weights approach zero.

For comparison, the usual low-energy approximation expands $\Sigma_S(E)$ around $E = 0$:

$$\begin{aligned} H_{\text{eff}} &= Z(h_w + \gamma_t\tau_x), \\ Z &= \left(1 + \frac{\gamma_t}{\Delta_S}\right)^{-1}. \end{aligned} \tag{49}$$

In this approximation, the bare perturbation is evaluated between unit-normalized eigenvectors of H_{eff}.

G. Kitaev-chain control

To identify which results depend on the semiconductor band structure, we repeat the excitation-kernel, population, coherence, and parameter-scan calculations for spinless Kitaev chains. The chains have the same length and lattice spacing as the Lutchyn–Oreg wire and couple to the same phonons through the same density vertex, $g_\lambda(x)\tau_z$.

In the basis $(c_j, c_j^\dagger)$, the Hamiltonian is

$$\begin{aligned} H_{jj} &= (2t - \mu_K)\tau_z, \\ H_{j,j+1} &= -t\tau_z + i\Delta_p\tau_y, \end{aligned} \tag{50}$$

with particle–hole conjugation $\tau_x K$. The zero-energy solutions have an envelope $e^{-\kappa x}$ and oscillate at wave vector k_0, where

$$\begin{aligned} \tanh(\kappa a) &= \frac{\Delta_p}{t}, \\ \cos(k_0 a) &= \frac{2t - \mu_K}{2\sqrt{t^2 - \Delta_p^2}}. \end{aligned} \tag{51}$$

Their bulk gap is $E_g = 2\Delta_p \sin(k_0 a)$. Specifying E_g, κ, and k_0 therefore fixes the three chain parameters t, μ_K, and Δ_p in closed form.

We construct two controls with different electronic momentum scales and label them low- and high-density chains. In the regime considered, k_0 tracks the Fermi momentum and hence the electron density. The low-density chain matches the wire's gap E_g, inverse Majorana decay length κ, and small oscillation wavevector k_0. The high-density chain retains the same E_g and κ but uses a larger k_0, corresponding to a shorter electronic wavelength and higher band filling. We extract κ and k_0 from its most slowly decaying oscillatory zero-energy solution,

$$e^{-x/\xi}\cos(k_0 x + \phi), \qquad \xi = 1/\kappa. \tag{52}$$

At the working point, this is also the slowest-decaying solution overall and determines the Majorana tail discussed in Sec. III A. In the scans of Sec. III F, we repeat

the matching at each V_Z and μ, using the gap and the most slowly decaying oscillatory solution at that point.

The high-density chain retains the same E_g and κ but sets $k_0 a = 1.25$. Its oscillation wavelength is approximately five lattice spacings, and $2k_0$ exceeds the wave vectors of all phonons considered here. This comparison tests how the electronic momentum scale affects phonon excitation at fixed gap and Majorana decay length.

III. RESULTS

Supplemental Tables S1–S6 collect the numerical results and checks.

A. Spectrum

The working point lies well inside the topological phase [Fig. 1(b)]. The finite wire has a bulk gap of 0.13 meV and a Majorana splitting of $\epsilon_M = 0.75$ μeV [Fig. 1(c)]. The end modes have tails that decay over $\xi = 355$ nm, while the lowest bulk mode extends across the wire [Fig. 1(d)]. The Fermi wavelength of about 330 nm reflects the low electron density. Spectrum and lattice-convergence checks are listed in Table S1.

B. Phonon excitation

The lowest allowed transitions create a Majorana-plus-bulk pair; creating two bulk quasiparticles requires more energy. Two thirds of the summed transition rates lie below 0.3 meV [Fig. 2(a)]. Promotion from an occupied Majorana level into the bulk has similar rates, giving the two logical states similar excitation probabilities (Table S1).

Momentum matching favors phonons traveling nearly perpendicular to the wire [Fig. 2(c)]. The electronic transition densities carry most of their Fourier weight below about $2k_F$, requiring $q|\cos\theta| \lesssim 2k_F$. Most coupling therefore comes from $\theta > 70°$, where $q_\perp \approx q$. Transverse confinement suppresses coupling to these phonons once $q_\perp R \gtrsim 1$, which accounts for the strong radius dependence in Fig. 2(b). The summed rates scale approximately as $R^{-4.3}$ over the range studied. Table S1 summarizes the branch-resolved rates, piezoelectric fractions, and field and chemical-potential scans. The different behavior near the two transitions is discussed in Sec. III F.

At equal excess energy density and pulse envelope, narrowband pulses excite the wire most efficiently just above threshold [Fig. 2(d)]. The efficiency is about 30 times smaller at 0.40 meV and nine orders of magnitude smaller at 1 meV. Both the electronic coupling and the phonon occupation per mode decrease with energy. For a narrow spectrum of fixed width, the latter scales as u/Ω_c^3. The broadband pulse places most of its energy above 0.5 meV, making it much less effective than the thermal pulse at the same energy density (Tables S1 and S3). Deposited energy alone therefore does not determine excitation.

C. Leakage, parity recovery, and poisoning

Phonons conserve wire parity. They can change the Majorana occupation while bulk quasiparticles are present. Once the bulk empties, the initial Majorana occupation must return if no quasiparticles have entered or left the wire. A simplified two-mode model illustrates this constraint.

Figure 3(a) compares exact and factorized kinetics for two modes restricted to $(0,0)$ and $(1,1)$ occupations. The blue solid curve is the exact occupation $f_0 = f_1 = P_{11}$, which also equals the joint occupation $\langle n_0 n_1 \rangle$. It obeys $\dot{P}_{11} = r_+(1 - P_{11}) - r_- P_{11}$. The gray dotted curve is the product of these exact mean occupations, $f_0 f_1 = P_{11}^2$, which is much smaller than the true joint occupation at low excitation probability.

The orange dashed curve is the occupation obtained from the factorized kinetic equation, $\dot{f} = r_+(1-f)^2 - r_- f^2$, with $f_0 = f_1 = f$. Replacing the joint occupation by a product underestimates recombination, so factorized kinetics overestimates the occupation.

For the 0.20-meV pulse, exact leakage and Majorana flips rise together and then decay [Fig. 3(b)]. Factorized kinetics instead leaves a spurious residual $f_0 \simeq 2P_{\rm exc}$. It also miscounts Pauli blocking: the approximation allows the bulk partner to enter the Majorana level, even though that level is occupied whenever the pair is present. The initial Majorana occupation recovers for all seven spectra and for either initial occupation, with a mean post-pulse return time of about 130 ns (Table S3).

Recombination in a large superconductor accelerates with quasiparticle density [19, 20]. Here, correlated pairs recombine at an almost fixed rate. The exact $P_{\rm flip}/u$ curves coincide [Fig. 3(c)], and the return time changes little over five decades of energy density. Table S2 lists equilibrium checks and the dependence on phonon energy density.

Permanent poisoning requires quasiparticle exchange. If a bulk partner escapes before recombination, a Majorana-plus-bulk excitation leaves the Majorana occupation reversed [Fig. 3(d)]. The poisoned fraction grows linearly with the escape rate when escape is slow and saturates at the Majorana-plus-bulk share of excitations. Without escape, it vanishes; factorized kinetics still predicts roughly two residual flips per excitation.

D. Logical coherence

Coherence remains lost after occupation recovery when the exchanged phonons reveal the logical state. Pair creation from an empty Majorana level exchanges energy $E_a + \epsilon_M$, whereas promotion from an occupied level exchanges $E_a - \epsilon_M$. At the working point, $\hbar/(2\epsilon_M) =$

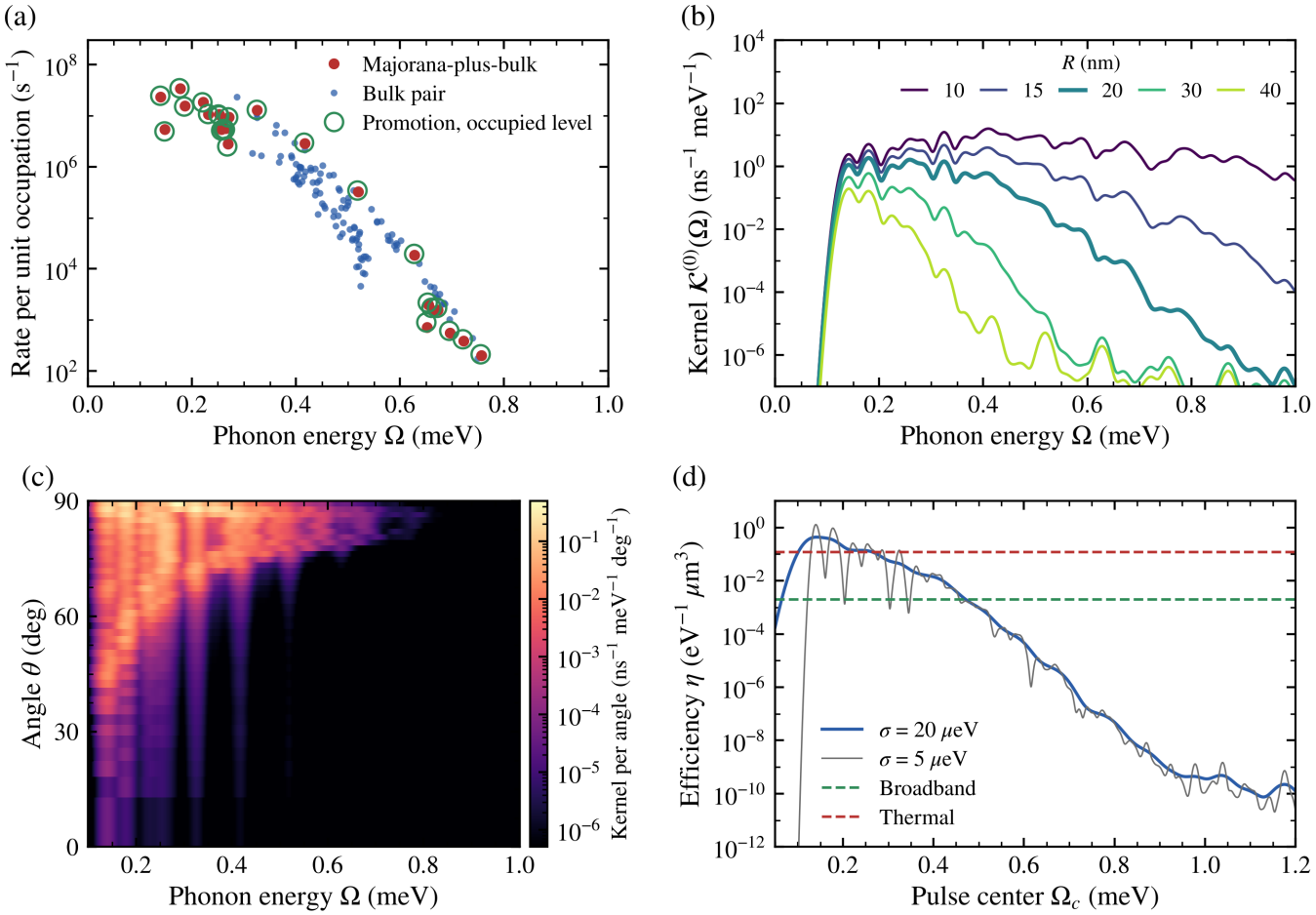

FIG. 2. Excitation kernel and pulse efficiency at the working point. (a) Cumulative transition rates: total, Majorana-plus-bulk and bulk-pair contributions for an empty Majorana level, and total for an occupied level, normalized to the empty-level total. (b) Kernels for transverse radii $R = 10$–40 nm. (c) Angular kernel, with θ measured from the wire axis and folded onto 0°–90°. (d) Weak-pulse efficiency η for narrowband spectra of bandwidth σ. Dashed lines show $-\ln(1 - P_{\rm exc})/u$ for broadband and thermal pulses (Table S3).

0.44 ns is much shorter than the excited-state lifetime, so the exchanged phonons are distinguishable in energy. For the 0.20-meV pulse, the blue solid curve in Fig. 4(a), $[1 - \chi_\varnothing(t)]/\bar{P}_{\rm exc}$, uses $\bar{P}_{\rm exc} = (P^{(0)}_{\rm exc} + P^{(1)}_{\rm exc})/2$ and rises during the pulse to a plateau near unity. The blue dashed leakage curve subsequently decays to zero, while the coherence loss remains at this plateau. Bulk relaxation therefore restores the code-space population but leaves a coherence loss $1 - \chi \simeq \bar{P}_{\rm exc}$. Complete dephasing of an excited path corresponds to a logical phase flip with probability 1/2 [31].

Bulk-pair creation initially acts identically on both logical states. Coherence survives direct recombination, but is lost if relaxation involves the Majorana level. Most bulk pairs take this second route, giving a final loss of $(0.75$–$1.00)\bar{P}_{\rm exc}$ across the seven spectra [Fig. 4(b), Table S3]. The transient overshoot in panel (a) reflects coherence carried by excited configurations and recovered during relaxation. Independent wires contribute additively at small loss. Escape changes poisoning much more strongly than coherence, since Majorana-plus-bulk paths have already dephased (Table S4).

Reducing ϵ_M removes the energy distinction, but mirror symmetry still makes the two phonon states orthogonal. In a uniform wire, reflection combined with σ_x makes $M^B_{a0}(k)M^A_{a0}(k)^*$ odd in k, so the cross kernel vanishes (Appendix B). The loss therefore persists as $\epsilon_M \to 0$ [Fig. 4(c)].

A gate gradient breaks this symmetry and concentrates bulk states near one end. Both logical branches can then couple to overlapping phonon states (Table S4). Coherence loss then decreases when $2\epsilon_M$ falls below the decay width. For the 0.15-meV pulse, the crossover is near $\epsilon_M = \hbar\Gamma_1/2 \simeq 10$ neV, with Γ_1 the lowest excitation's decay rate. Figure 4(c) shows each curve normalized to its own loss at $\epsilon_M = 1$ μeV because the gate gradient also changes the excitation probability. At the working point, $2\epsilon_M/\hbar$ greatly exceeds the transition rates, so the

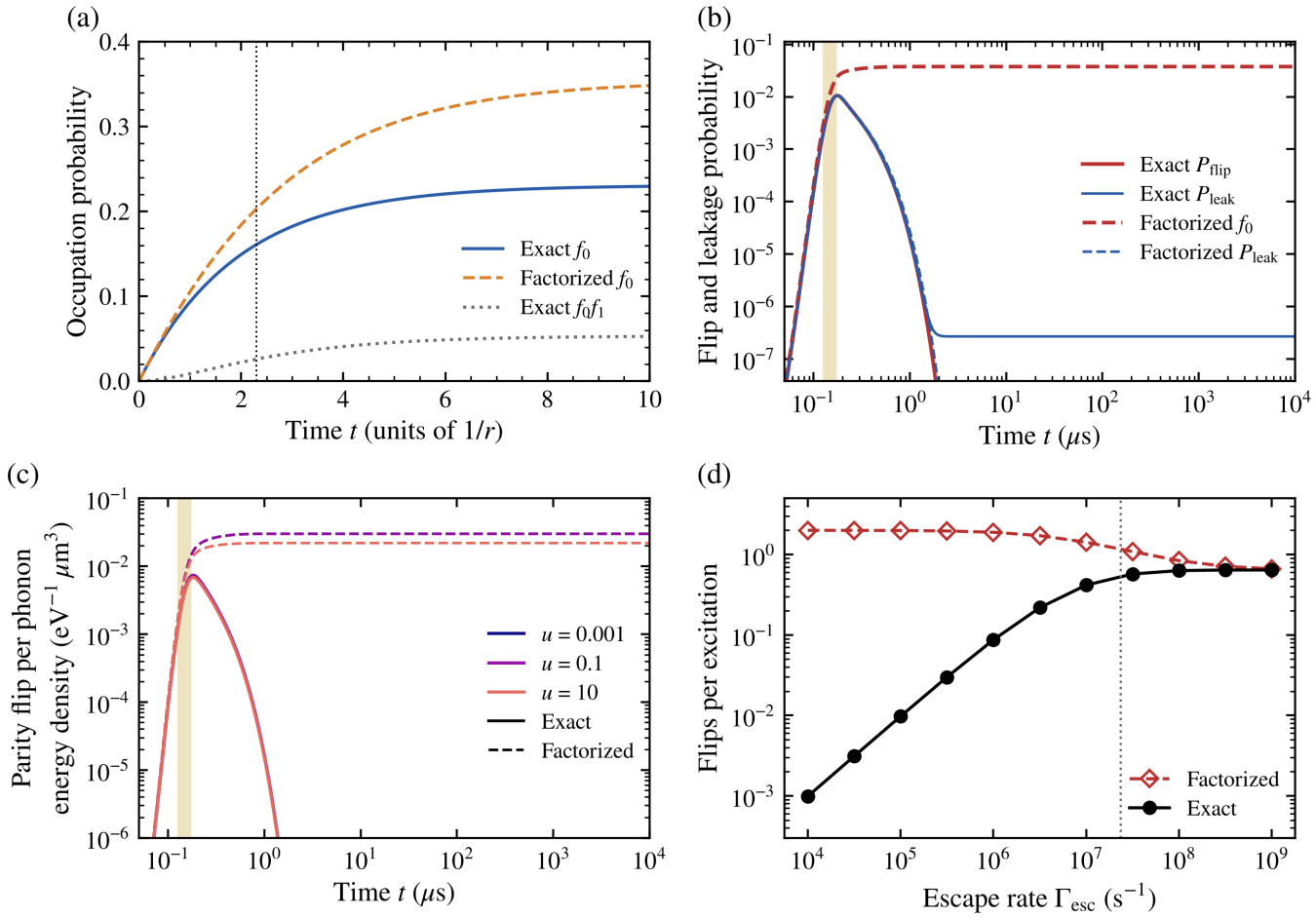

FIG. 3. Leakage, parity recovery, and poisoning. (a) Two-mode pair dynamics with $r_+ = 0.12r$ and $r_- = 0.40r$: exact occupation $f_0 = f_1 = P_{11} = \langle n_0 n_1 \rangle$, factorized occupation, and product of the exact mean occupations. (b) A 0.20-meV pulse at $u = 0.1$ eV μm^{-3}: exact $P_{\rm flip}$ and $P_{\rm leak}$ (solid), factorized f_0 and leakage (dashed). Shading marks the pulse FWHM; the late leakage plateau represents discarded probability beyond $k_{\rm max} = 2$. (c) Exact $P_{\rm flip}/u$ and factorized f_0/u for a broadband 0.1–0.6 meV pulse at three energy densities (17 modes, $k_{\rm max} = 4$). (d) Residual flips per excitation at 10 ms versus escape rate for the broadband 0.1–1.0 meV pulse at the reference energy density. The dotted line marks the lowest pair's recombination rate, 2.35×10^7 s^{-1}.

cross terms coupling χ_S to $\chi^*_{S\pm a}$ average out.

E. Hybrid normalization

We compare excitation rates from the effective model with rates calculated by including the parent superconductor explicitly. The ratio γ_t/Δ_S measures the wire–parent tunnel-coupling energy scale relative to the parent gap. Increasing this ratio strengthens hybridization and shifts more of a low-energy state's weight into the parent. Figure 5(a) shows the semiconductor weight Z_a versus state energy for three coupling strengths. The phonon coupling considered here acts only in the semiconductor, so matrix elements acquire $\sqrt{Z_a Z_b}$ and rates acquire $Z_a Z_b$. At low energies, $Z_a \approx Z(0) = (1 + \gamma_t/\Delta_S)^{-1}$.

Figure 5(b) compares three excitation kernels at $\gamma_t = \Delta_S$. The gray curve uses unit-normalized effective states with the bare phonon vertex, assigning their entire weight to the semiconductor. The blue dashed curve corrects the phonon vertex using the constant factor $Z(0)^2 = 1/4$, while the red curve uses the exact hybrid states and their individual semiconductor weights. Near threshold, hybrid normalization reduces the kernel approximately fourfold. Including hybridization therefore weakens phonon excitation of the wire.

F. Electronic structure effects

We compare the Lutchyn–Oreg wire with Kitaev chains matched to its gap and Majorana decay length to identify which results depend on the semiconductor band structure. The Kitaev chains reproduce parity recovery,

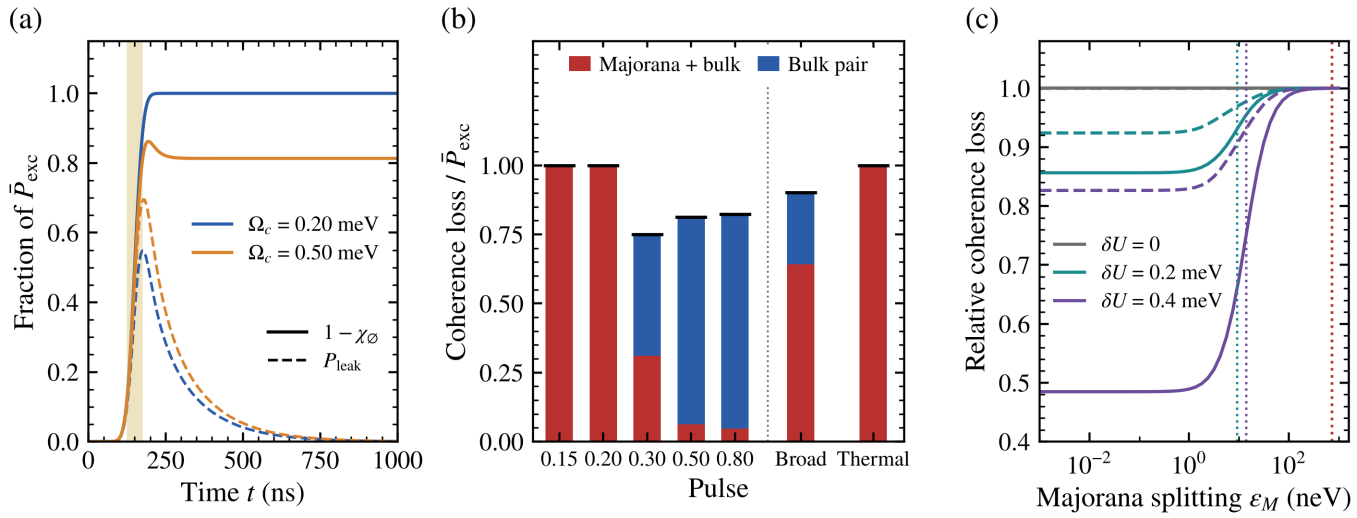

FIG. 4. Logical coherence and mirror symmetry (rapidly oscillating coherence-transfer terms neglected in a,b). (a) Code-space coherence loss (solid) and leakage from the initially empty-Majorana branch (dashed), normalized to the branch-averaged excitation probability $\bar{P}_{\rm exc}$, for 0.20- and 0.50-meV pulses at $u = 0.1$ eV μm^{-3}. Shading marks the pulse FWHM. (b) Final loss per excitation for the seven spectra in Table S3, resolved into Majorana-plus-bulk and bulk-pair paths involving the Majorana level. (c) Loss versus splitting, varied at fixed wave functions to first order in u and normalized to each wire's loss at $\epsilon_M = 1$ μeV. Solid and dashed curves show 0.15- and 0.20-meV pulses, respectively, for a uniform wire and gate gradients $U(x) = \delta U(x/L - 1/2)$. Dotted lines mark $\hbar\Gamma_1/2$ for the gradient wires and the working-point splitting.

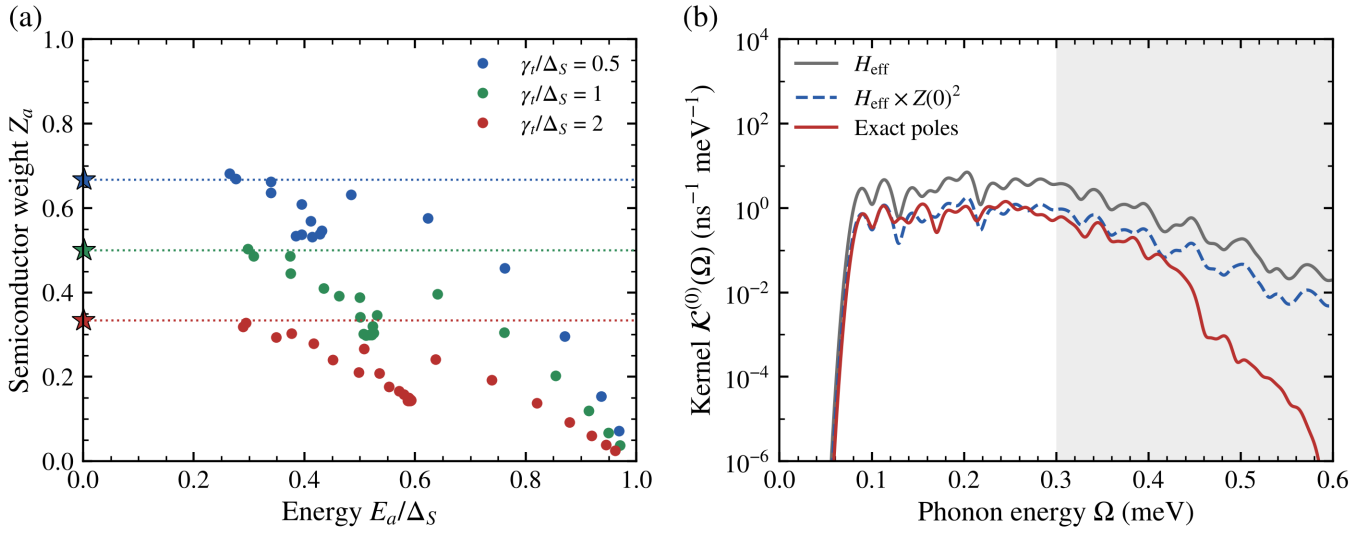

FIG. 5. Semiconductor weight and its effect on phonon excitation. The parent superconducting gap is $\Delta_S = 0.30$ meV. (a) Semiconductor weight Z_a versus bound-state energy for $\gamma_t/\Delta_S = 0.5$, 1, and 2. Stars identify the Majorana-derived states; dotted lines show the low-energy approximation $Z(0) = (1 + \gamma_t/\Delta_S)^{-1}$. (b) Excitation kernel $\mathcal{K}^{(0)}(\Omega)$ for $\gamma_t = \Delta_S$, calculated using three approaches: the effective Hamiltonian $H_{\rm eff}$ with unit-normalized eigenstates (gray); the same kernel multiplied by $Z(0)^2$ (blue dashed); and the hybrid bound states, with phonons coupled to their semiconductor components $w_a = \sqrt{Z_a}\varphi_a$ (red). Here φ_a is normalized to one. The shaded region marks energies above the parent gap, where transitions into the parent continuum become possible. These transitions are omitted from the calculation.

the failure of factorized kinetics, and excitation-induced coherence loss, with recovery times of the same order of magnitude as the wire's (Table S6). These results follow from parity conservation, pair correlations, and the ability of phonons to distinguish the logical states. Uniform Kitaev chains also have vanishing cross kernels by reflection symmetry.

Excitation efficiencies depend more strongly on elec-

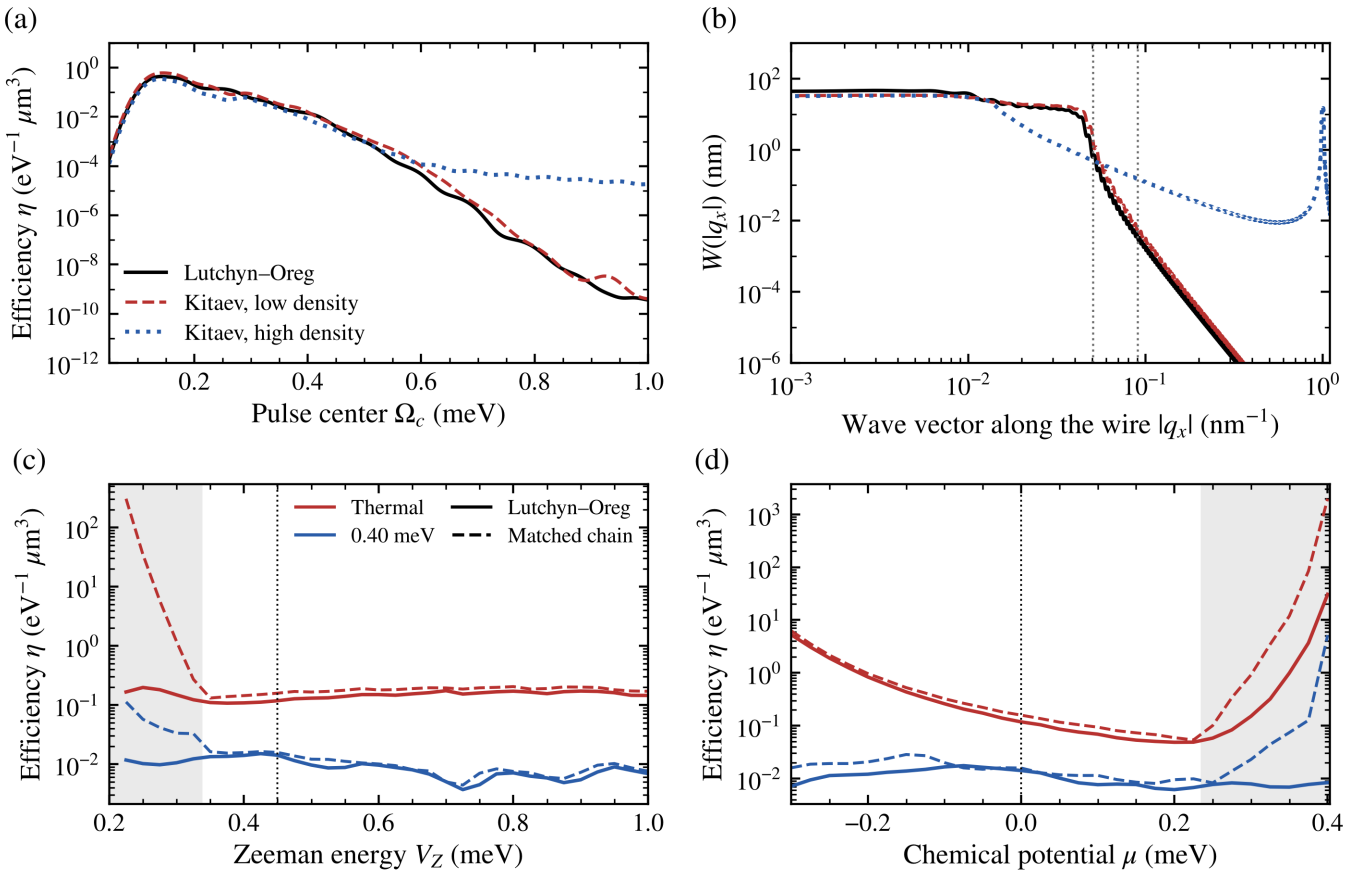

FIG. 6. Lutchyn–Oreg wire and Kitaev chains matched to its gap and Majorana decay length, at low ($k_0 = 0.0184$ nm^{-1}) and high ($k_0 a = 1.25$) density. (a) Narrowband excitation efficiency for $\sigma = 20$ μeV. (b) Fourier weight of Majorana-plus-bulk transition densities below 0.6 meV, normalized to unit area. Dotted lines mark LA and TA wave vectors at threshold. (c),(d) Thermal and 0.40-meV efficiencies versus field and chemical potential, compared with low-density chains matched at each point. Shading marks a gap minimum at $k = 0$; dotted lines mark the working point.

tronic structure. Below 0.5 meV, the low-density chain agrees with the nanowire within a factor of 1.6, whereas at 1 meV the high-density chain is 5×10^4 more efficient than the nanowire [Fig. 6(a)]. Figure 6(b) shows the normalized, symmetrized Fourier weight for Majorana–bulk pair creation, $W(|q_x|) = \frac{S(|q_x|)+S(-|q_x|)}{\int_0^{q_{\max}} [\,S(q)+S(-q)\,]\,dq}$, where $S(k) = \sum_{a\geq 1:\, E_a+\epsilon_M \leq 0.6\,\mathrm{meV}} |M^B_{0a}(k)|^2$, M^B_{0a} is the Fourier transform of the pair-creation transition density defined in Eq. (11), and $q_{\max} = 0.9\pi/a = 1.13$ nm^{-1}. In the low-density chain, the densities governing electron–phonon transitions vary smoothly near the ends, so their Fourier transforms contain little weight at large longitudinal wavevectors. In the high-density chain, sharper spatial variations near the hard-wall boundaries produce substantial high-momentum Fourier weight [Fig. 6(b)]. Energetic acoustic phonons have large wavevectors. Those propagating along the chain can couple to these high-momentum components, while the transverse form factor suppresses coupling to transverse phonons. Smoothing the high-density chain's transition densities near the ends removes much of this Fourier weight and strongly reduces the excitation efficiency (Table S6).

Fitting the gap, decay length, and Fermi momentum reproduces efficiencies within about a factor of two while the gap minimum lies near k_F [Figs. 6(c),(d)]. We obtain the Kitaev chain's dependence on V_Z by matching its parameters to the wire. At each V_Z, we extract the wire's bulk gap E_g and the decay length ξ and wavevector k_0 of its slowest-decaying oscillatory zero-energy solution. These three quantities determine t, μ_K, and Δ_p in the Kitaev chain model. Near the topological transition, the wire's lowest-energy bulk excitations occur near $k = 0$, while the Majorana mode's spatial oscillations are still determined by states near k_F. The matched Kitaev chain cannot reproduce both features simultaneously. It predicts too many low-energy bulk states and overestimates the thermal excitation efficiency by three orders of magnitude (Table S6).

The field-driven and chemical-potential-driven transitions also differ. A small gap makes excitation energetically accessible, although selection rules can suppress phonon coupling. At $k = 0$ in the topological phase, the

two positive-energy states have the same spin, so spin-conserving density coupling cannot create a pair in them. Near $\mu = 0$, the spin and electron–hole structure of the low-energy states nearly suppresses their phonon-induced pair-creation matrix elements, even at small nonzero momentum. Moving μ away from zero changes this structure and allows stronger pair creation, even for the same excitation gap. Thus, lowering V_Z to reduce the gap to 25 μeV changes the thermal-pulse efficiency by less than a factor of two, while tuning μ to reach the same gap increases the efficiency to 31 times its working-point value [Figs. 6(c),(d), Table S6]. Phonon sensitivity therefore depends on the states' spin and particle–hole structure as well as their excitation energies.

IV. SUMMARY AND OUTLOOK

Phonon-induced excitations can relax without restoring the quantum information stored in a Majorana qubit. Without quasiparticle exchange with the environment, wire parity is conserved, so the initial Majorana occupation is restored when the bulk empties. The mean post-pulse return time is about 130 ns in the Lutchyn–Oreg wires studied here. Factorized Boltzmann kinetics misses the pair correlations and instead leaves a spurious residual Majorana occupation of about $2P_{\mathrm{exc}}$ for an initially empty level under a weak pulse. Despite occupation recovery, the exchanged phonons usually distinguish the logical states. For the seven spectra studied, the fractional coherence loss per wire is 0.75–1.00 times its branch-averaged excitation probability. These mechanisms also occur in the matched Kitaev chains. Reducing the Majorana splitting makes the phonons exchanged by the two logical states closer in energy. In a mirror-symmetric wire, however, their different spatial patterns still reveal the logical state. Breaking this symmetry allows the phonon states to overlap, so a sufficiently small splitting can reduce coherence loss.

The excitation probability depends strongly on both the phonon spectrum and the electronic structure. At equal phonon energy density and pulse envelope, spectra concentrated near threshold cause far more excitation than higher-energy spectra. Low electron density suppresses coupling to energetic phonons, while a selection rule near the field-driven transition weakens coupling to the modes whose gap closes. Changing the chemical potential weakens this approximate protection away from $k = 0$, so wires with the same bulk gap can have very different excitation probabilities. Accounting for the semiconductor weight of hybrid states reduces near-threshold excitation rates by about fourfold relative to the bare-vertex calculation when $\gamma_t = \Delta_S$.

Quantitative device predictions will require band structures and interface tunneling appropriate to the device geometry [39], microscopic electron–phonon couplings [13, 40], and phonon modes of the wire, shell, and substrate. Coupling within the superconducting shell and transitions into its continuum must also be included [13]. Further extensions should address multiband and orbital effects, realistic confinement, the superconducting backbone and island charging energy, correlations between wires exposed to a shared phonon field, and corrections to the Born–Markov treatment. Combining these kinetics with substrate and interface phonon transport, bath back-action, and microscopic escape channels would connect an ionizing event to qubit errors. By linking nonequilibrium phonon spectra to quasiparticle dynamics and the survival of quantum information, this framework provides a microscopic foundation for assessing radiation-induced errors and guiding the design of more resilient Majorana qubits.

DATA AVAILABILITY

The code and data supporting this article are available from the author upon reasonable request.

Appendix A: Model parameters and numerical settings

The default nanowire parameters are $m^* = 0.023\, m_e$, $\alpha = 20$ meV nm, $\mu = 0$, $V_Z = 0.45$ meV, $\Delta = 0.20$ meV, $L = 2$ μm, and $a = 2.5$ nm. The two parallel wires are separated by $d = 300$ nm and have no tunneling between them. For the phonons, we use the mass density $\rho = 5.667\ \mathrm{g\,cm^{-3}}$, Voigt-averaged sound velocities $c_L = 4.195$ and $c_T = 2.352\ \mathrm{km\,s^{-1}}$, and LA deformation potential $D = 5.08$ eV [41]. The unscreened piezoelectric coupling uses $e_{14} = 0.045\ \mathrm{C\,m^{-2}}$ and $\varepsilon_r = 15.15$ [42]. The wire axis is [111], and the Gaussian transverse electron density has radius $R = 20$ nm.

The bath is isotropic and incoherent at $T_{\mathrm{bath}} = 20$ mK. Pulses have a Gaussian time envelope centered at 150 ns with a full width at half maximum of 50 ns. The narrowband spectrum is Gaussian with standard deviation $\sigma = 20$ μeV and center Ω_c; the broadband spectrum has uniform excess occupation from 0.1 to 1.0 meV; and the thermal spectrum is the excess Bose occupation at $T^* = 311$ mK over the 20-mK bath. The reference peak excess energy density is $u = 0.1\ \mathrm{eV}\,(\mu\mathrm{m})^{-3}$, equivalent to 10 keV distributed within a cube of side 46 μm.

The main kinetic calculation retains 34 quasiparticle modes below 1.2 meV and configurations with at most $k_{\max} = 2$ bulk quasiparticles. The scan over phonon energy density uses 17 modes and $k_{\max} = 4$. Retaining the coherences of 301 near-degenerate configuration pairs changes the time-integrated leakage by a relative $\leq 10^{-5}$. Plotted excitation kernels are broadened with a Gaussian of standard deviation 10 μeV, reduced to 6 μeV for the parent-superconductor comparison. That comparison uses $\Delta_S = 0.30$ meV, $\gamma_t/\Delta_S = 0.5$, 1, and 2, $V_{Z,\mathrm{bare}} = 2.25\gamma_t$, lattice spacing $a = 5$ nm, and bound states with $E < 0.97\Delta_S$. The Kitaev-chain parameters

(t, μ_K, Δ_p) are $(194, 0.42, 1.37)$ meV for the low-density control and $(9.4, 12.9, 0.066)$ meV for the high-density control. The latter has $k_0 a = 1.25$ and $2k_0 = 1.0\ \mathrm{nm}^{-1}$, exceeding the wave vectors of phonons with energies up to 1.5 meV.

Appendix B: Phonon-state overlap and logical coherence

Here we expand the overlap in Eq. (35) and distinguish the coherence loss along an excitation path from the loss averaged over a pulse. The comparison uses the common phonon energy $\Omega = E_a$; the physical pair-creation and promotion energies are $E_a + \epsilon_M$ and $E_a - \epsilon_M$, respectively.

1. Direct and cross coefficients

Set $u = \cos\theta$ and $q_\nu = E_a/(\hbar c_\nu)$. All three coefficients contain the same nonnegative angular weight,

$$w_\nu(u) = \frac{q_\nu}{8\pi^2 \hbar \rho c_\nu^2} \bar{C}_\nu(\arccos u, q_\nu) \times \left| F_\perp\left(q_\nu \sqrt{1-u^2}\right)\right|^2 \geq 0. \quad \text{(B1)}$$

Writing out the direct and cross coefficients gives

$$\Gamma_a^A = \sum_\nu \int_{-1}^{1} du\, w_\nu(u) |M_{a0}^A(q_\nu u)|^2, \quad \text{(B2)}$$

$$\Gamma_a^B = \sum_\nu \int_{-1}^{1} du\, w_\nu(u) |M_{a0}^B(q_\nu u)|^2, \quad \text{(B3)}$$

$$\Gamma_a^\times = \sum_\nu \int_{-1}^{1} du\, w_\nu(u) M_{a0}^B(q_\nu u) M_{a0}^A(q_\nu u)^*. \quad \text{(B4)}$$

The direct coefficients sum squared amplitudes, whereas the cross coefficient sums their complex products. The cross contributions can cancel between phonon directions even when both direct coefficients are nonzero.

For $\Gamma_a^A, \Gamma_a^B > 0$, define the normalized mode amplitudes

$$f_\nu^X(u) = \frac{\sqrt{w_\nu(u)}\, M_{a0}^X(q_\nu u)}{\sqrt{\Gamma_a^X}}, \qquad X = A, B. \quad \text{(B5)}$$

Equations (B2) and (B3) imply

$$\sum_\nu \int_{-1}^{1} du\, |f_\nu^X(u)|^2 = 1. \quad \text{(B6)}$$

Substitution into Eq. (35) then yields

$$\kappa_a = \left| \sum_\nu \int_{-1}^{1} du\, f_\nu^A(u)^* f_\nu^B(u) \right| = |\langle f^A | f^B \rangle|. \quad \text{(B7)}$$

Thus κ_a is the magnitude of a normalized inner product, so the Cauchy–Schwarz inequality gives $\kappa_a \leq 1$. A zero value means that the mode profiles are orthogonal; unity means that their normalized profiles are identical up to a common phase.

These expressions exclude phonon occupations. The same construction applies to absorption or emission coefficients if $w_\nu(u)$ is replaced everywhere by $w_\nu(u) N_\nu(E_a, t)$ or $w_\nu(u)[N_\nu(E_a, t)+1]$, respectively. The bound requires the same energy and weighting in the two direct coefficients and their cross coefficient.

2. Cancellation from mirror symmetry

Choose the coordinate origin at the wire center. For the uniform Lutchyn–Oreg wire, reflection combined with σ_x, denoted by $\mathcal{R} = \sigma_x \mathcal{P}_x$, commutes with the Hamiltonian. Eigenstates can therefore be chosen with $\mathcal{R}\Phi_j = r_j \Phi_j$, where $r_j = \pm 1$. Particle–hole conjugation anticommutes with this reflection, so

$$\mathcal{R}\mathcal{C}\Phi_0 = -r_0 \mathcal{C}\Phi_0. \quad \text{(B8)}$$

Since the density vertex τ_z is invariant under the reflection, the two transition densities have opposite reflection parity:

$$\begin{aligned} \rho_{a0}^A(-x) &= r_a r_0\, \rho_{a0}^A(x), \\ \rho_{a0}^B(-x) &= -r_a r_0\, \rho_{a0}^B(x). \end{aligned} \quad \text{(B9)}$$

Their Fourier transforms consequently obey

$$\begin{aligned} M_{a0}^A(-k) &= r_a r_0\, M_{a0}^A(k), \\ M_{a0}^B(-k) &= -r_a r_0\, M_{a0}^B(k). \end{aligned} \quad \text{(B10)}$$

The cross product is therefore odd in longitudinal momentum:

$$M_{a0}^B(-k) M_{a0}^A(-k)^* = -M_{a0}^B(k) M_{a0}^A(k)^*. \quad \text{(B11)}$$

For the reflection-symmetric phonon weighting used here, $w_\nu(-u) = w_\nu(u)$. The integral in Eq. (B4) vanishes, giving $\Gamma_a^\times = 0$ and $\kappa_a = 0$. Breaking mirror symmetry removes this cancellation and permits a nonzero overlap, whose magnitude must be calculated from the resulting wave functions.

The common-energy overlap describes the phonon mode profiles. It does not account for the distinguishability of phonons with different energies $E_a \pm \epsilon_M$. Thus $\kappa_a = 1$ alone does not guarantee coherence preservation: the energy difference and the two branch rates also matter.

3. Orthogonal phonons and pulse-averaged dephasing

A vanishing κ_a removes the coherence-transfer term for the corresponding transition; it does not set the entire logical coherence to zero. Orthogonal phonon states

retain information about the logical branch along that excitation path. The pulse-averaged loss also depends on how often that path is taken.

For illustration, suppose that an excursion completely dephases the qubit with the same probability $P_{\rm d}$ on both logical branches, while the remaining events leave it unchanged. After recovery,

$$\begin{aligned}\rho_{01}^{f} &= (1-P_{\rm d})\rho_{01}^{i},\\ D &= 1-\frac{|\rho_{01}^{f}|}{|\rho_{01}^{i}|} = P_{\rm d}.\end{aligned} \tag{B12}$$

Even complete dephasing along every excited path therefore produces only a small average loss when those paths are rare. For example, $P_{\rm d}=0.01$ gives a 1% coherence loss. The excitation probability determines how often the wire leaves its empty-bulk state, whereas κ_a helps determine whether particular transitions preserve the coherence carried by those excursions. Bulk pairs that recombine without involving the Majorana level can return coherence to the code space. The final loss must therefore be obtained from the coupled χ_S dynamics rather than from κ_a or $P_{\rm exc}$ alone.

Appendix C: Coefficient matrices and coherence evolution

The two-channel matrices in Eq. (37) act on transition operators. Their off-diagonal entries describe interference between the pair-creation and promotion amplitudes. This appendix gives their explicit form and the conditions for completely positive evolution.

1. Direct and cross terms

Before including phonon occupations, the common-energy matrix in the ordered channel basis (B, A) is

$$\mathsf{C}_a^{(0)} = \begin{pmatrix} \Gamma_a^B & \Gamma_a^{\times} \\ (\Gamma_a^{\times})^* & \Gamma_a^A \end{pmatrix}. \tag{C1}$$

The operators are $F_{aB}^{+} = c_a^{\dagger}c_0^{\dagger}$ and $F_{aA}^{+} = c_a^{\dagger}c_0$, with reverse operators $F_{aX}^{-} = (F_{aX}^{+})^{\dagger}$. For example, the absorption contribution is

$$\mathcal{D}_a^{+}[\rho] = \sum_{X,Y\in\{B,A\}} (\mathsf{C}_a^{+})_{XY} \times \left(F_{aX}^{+}\rho F_{aY}^{+\dagger} - \frac{1}{2}\{F_{aY}^{+\dagger}F_{aX}^{+},\rho\}\right). \tag{C2}$$

The terms $X=Y$ are the ordinary pair-creation and promotion channels; $X\neq Y$ transfer coherence between the corresponding configurations.

Write $\mathsf{C}_{a\nu}^{(0)}$ for the branch-ν contribution to Eq. (C1), with every entry evaluated at E_a. A consistent common-energy construction including phonon occupations is

$$\begin{aligned}\widetilde{\mathsf{C}}_a^{+}(t) &= \sum_{\nu} N_{\nu}(E_a,t)\mathsf{C}_{a\nu}^{(0)},\\ \widetilde{\mathsf{C}}_a^{-}(t) &= \sum_{\nu} [N_{\nu}(E_a,t)+1]\mathsf{C}_{a\nu}^{(0)*}.\end{aligned} \tag{C3}$$

The second line is complex conjugated because emission uses the conjugate microscopic amplitudes and the adjoint transition operators. The tilde distinguishes this common-energy construction from a matrix whose diagonal entries retain the physical transition energies $E_a \pm \epsilon_M$.

2. Positivity and its energy convention

For the matrix in Eq. (C1), the diagonal entries are nonnegative and

$$\begin{aligned}\det \mathsf{C}_a^{(0)} &= \Gamma_a^A\Gamma_a^B - |\Gamma_a^{\times}|^2\\ &= \Gamma_a^A\Gamma_a^B(1-\kappa_a^2) \geq 0.\end{aligned} \tag{C4}$$

Together these conditions make the Hermitian 2×2 matrix positive semidefinite. Equivalently, its eigenvalues are

$$\lambda_{\pm} = \frac{1}{2}\left[\Gamma_a^A + \Gamma_a^B \pm\sqrt{(\Gamma_a^A-\Gamma_a^B)^2 + 4|\Gamma_a^{\times}|^2}\right] \geq 0. \tag{C5}$$

The same argument holds for each phonon branch separately. Multiplication by the nonnegative Bose factors and summation over branches therefore preserve positivity in Eq. (C3).

More generally, for the matrices with diagonal rates $d_{aX}^{\pm}$ and cross coefficients $r_a^{\pm}$ in Eq. (37), positivity holds if and only if

$$d_{aA}^{\pm} \geq 0, \qquad d_{aB}^{\pm} \geq 0, \qquad |r_a^{\pm}|^2 \leq d_{aA}^{\pm} d_{aB}^{\pm}. \tag{C6}$$

The bare bound $\kappa_a \leq 1$ proves this inequality only when the direct and cross terms use the same energy and phonon weighting. If the diagonal rates instead use $E_a - \epsilon_M$ and $E_a + \epsilon_M$, while the cross term is evaluated at E_a, Eq. (C6) must be checked separately. It does not follow from the common-energy overlap alone. Equation (C3) gives a consistently positive common-energy block. When rapid oscillations suppress the cross terms, the separate physical rates give nonnegative diagonal matrices.

For any positive block, diagonalization $\mathsf{C} = U\,\mathrm{diag}(\lambda_r)U^{\dagger}$ gives jump operators

$$L_r = \sqrt{\lambda_r}\sum_X U_{Xr}F_X. \tag{C7}$$

Its contribution becomes $\sum_r [L_r \rho L_r^\dagger - \{L_r^\dagger L_r, \rho\}/2]$. The resulting time-local evolution is trace preserving and completely positive when all retained blocks are positive. This statement applies before configuration truncation, or to a space that includes the truncation sink. Discarding probability beyond the cutoff makes the retained block trace decreasing; its diagonal loss terms must still include the outgoing rates. A zero cross coefficient leaves two independent transition channels; it does not remove their direct rates. A rank-one positive block has one combined jump operator.

3. Configuration elements, phases, and the spectator wire

The component equation (42) follows by taking matrix elements of Eq. (40). Each allowed jump changes definite occupations. The products $F_{aA}^{+\dagger} F_{aB}^{+}$ and $F_{aB}^{+\dagger} F_{aA}^{+}$ vanish, as do the corresponding emission products. The anticommutator therefore contains a diagonal loss operator and contributes $-(\Lambda_n + \Lambda_m)\rho_{nm}/2$. The jump term gives $K_{nm;kl}\rho_{kl}$, including the signs generated by the fermionic ordering in Eq. (21). This construction also applies to escape jumps, whose coherence-transfer signs cannot be inferred from population rates alone.

The spectator occupation remains part of the full two-wire state label. Without escape, even total parity fixes the explicit version of the shorthand coherence in Eq. (32):

$$\chi_S = \frac{\langle 0, S; r_S|\rho|1, S; 1 - r_S\rangle}{C_0}, \qquad r_S = |S| \bmod 2, \tag{C8}$$

where the label after the semicolon is the partner wire's Majorana occupation and $C_0 = \rho_{01}(0) \neq 0$. At $S = \varnothing$, this is the original logical coherence between $|00\rangle$ and $|11\rangle$. It is not an off-diagonal element of the single-wire reduced density matrix. With escape, the total wire parity can change, so the partner occupation must be retained independently rather than inferred from r_S.

Finally, Hermiticity relates unnormalized density-matrix elements by $\rho_{mn} = \rho_{nm}^*$. For normalized coherences and a general complex C_0, this becomes

$$\frac{\rho_{mn}}{C_0} = \frac{C_0^*}{C_0}\left(\frac{\rho_{nm}}{C_0}\right)^*. \tag{C9}$$

A transfer term written only with χ_S^* therefore assumes real C_0; otherwise, it must retain the displayed phase factor. The component equation for ρ_{nm} is valid for either convention. Dividing by C_0 gives the normalized coherences.

[1] A. Y. Kitaev, Unpaired Majorana fermions in quantum wires, Phys.-Usp. **44**, 131 (2001).
[2] R. M. Lutchyn, J. D. Sau, and S. Das Sarma, Majorana fermions and a topological phase transition in semiconductor-superconductor heterostructures, Phys. Rev. Lett. **105**, 077001 (2010).
[3] Y. Oreg, G. Refael, and F. von Oppen, Helical liquids and Majorana bound states in quantum wires, Phys. Rev. Lett. **105**, 177002 (2010).
[4] J. Alicea, New directions in the pursuit of Majorana fermions in solid state systems, Rep. Prog. Phys. **75**, 076501 (2012).
[5] R. M. Lutchyn, E. P. A. M. Bakkers, L. P. Kouwenhoven, P. Krogstrup, C. M. Marcus, and Y. Oreg, Majorana zero modes in superconductor-semiconductor heterostructures, Nat. Rev. Mater. **3**, 52 (2018).
[6] M. Aghaee *et al.* (Microsoft Quantum), InAs-Al hybrid devices passing the topological gap protocol, Phys. Rev. B **107**, 245423 (2023).
[7] M. Aghaee *et al.* (Microsoft Azure Quantum), Interferometric single-shot parity measurement in InAs–Al hybrid devices, Nature **638**, 651 (2025).
[8] D. Rainis and D. Loss, Majorana qubit decoherence by quasiparticle poisoning, Phys. Rev. B **85**, 174533 (2012).
[9] T. Karzig, W. S. Cole, and D. I. Pikulin, Quasiparticle poisoning of Majorana qubits, Phys. Rev. Lett. **126**, 057702 (2021).
[10] C. D. Wilen *et al.*, Correlated charge noise and relaxation errors in superconducting qubits, Nature **594**, 369 (2021).
[11] M. McEwen *et al.*, Resolving catastrophic error bursts from cosmic rays in large arrays of superconducting qubits, Nat. Phys. **18**, 107 (2022).
[12] J. M. Martinis, Saving superconducting quantum processors from decay and correlated errors generated by gamma and cosmic rays, npj Quantum Inf. **7**, 90 (2021).
[13] H. Huang, S. Kielar, and Z. Tian, Ab initio calculation of nonequilibrium quasiparticle-phonon dynamics in superconductors, AVS Quantum Sci. **6**, 016201 (2024).
[14] P. P. Aseev, P. Marra, P. Stano, J. Klinovaja, and D. Loss, Degeneracy lifting of Majorana bound states due to electron-phonon interactions, Phys. Rev. B **99**, 205435 (2019).
[15] Y. Song and S. Das Sarma, Phonon-induced Majorana qubit relaxation in tunnel-coupled two-island topological superconductors, Phys. Rev. B **98**, 075159 (2018).
[16] C. Knapp, T. Karzig, R. M. Lutchyn, and C. Nayak, Dephasing of Majorana-based qubits, Phys. Rev. B **97**, 125404 (2018).
[17] O. Kaestle, Y. Sun, Y. Hu, and A. Carmele, Memory-critical dynamical buildup of phonon-dressed Majorana fermions, Phys. Rev. B **102**, 245115 (2020).
[18] E. Yelton, C. P. Larson, V. Iaia, K. Dodge, G. La Magna, P. G. Baity, I. V. Pechenezhskiy, R. McDermott, N. Kurinsky, G. Catelani, and B. L. T. Plourde, Modeling phonon-mediated quasiparticle poisoning in superconducting qubit arrays, Phys. Rev. B **110**, 024519 (2024).
[19] A. Rothwarf and B. N. Taylor, Measurement of recombination lifetimes in superconductors, Phys. Rev. Lett. **19**, 27 (1967).

[20] S. B. Kaplan, C. C. Chi, D. N. Langenberg, J. J. Chang, S. Jafarey, and D. J. Scalapino, Quasiparticle and phonon lifetimes in superconductors, Phys. Rev. B **14**, 4854 (1976).

[21] C. M. Wilson and D. E. Prober, Quasiparticle number fluctuations in superconductors, Phys. Rev. B **69**, 094524 (2004).

[22] V. F. Maisi, S. V. Lotkhov, A. Kemppinen, A. Heimes, J. T. Muhonen, and J. P. Pekola, Excitation of single quasiparticles in a small superconducting Al island connected to normal-metal leads by tunnel junctions, Phys. Rev. Lett. **111**, 147001 (2013).

[23] D. G. Olivares, A. Levy Yeyati, L. Bretheau, Ç. Ö. Girit, H. Pothier, and C. Urbina, Dynamics of quasiparticle trapping in Andreev levels, Phys. Rev. B **89**, 104504 (2014).

[24] F. L. Pedrocchi and D. P. DiVincenzo, Majorana braiding with thermal noise, Phys. Rev. Lett. **115**, 120402 (2015).

[25] F. L. Pedrocchi, N. E. Bonesteel, and D. P. DiVincenzo, Monte Carlo studies of the properties of the Majorana quantum error correction code: Is self-correction possible during braiding?, Phys. Rev. B **92**, 115441 (2015).

[26] M. Ippoliti, M. Rizzi, V. Giovannetti, and L. Mazza, Quantum memories with zero-energy Majorana modes and experimental constraints, Phys. Rev. A **93**, 062325 (2016).

[27] N. Breckwoldt, T. Posske, and M. Thorwart, Bath-induced decoherence in finite-size Majorana wires at nonzero temperature, New J. Phys. **24**, 013033 (2022).

[28] M. J. Schmidt, D. Rainis, and D. Loss, Decoherence of Majorana qubits by noisy gates, Phys. Rev. B **86**, 085414 (2012).

[29] M. Cheng, R. M. Lutchyn, and S. Das Sarma, Topological protection of Majorana qubits, Phys. Rev. B **85**, 165124 (2012).

[30] A. Alase, M. C. Goffage, M. C. Cassidy, and S. N. Coppersmith, Decoherence of Majorana qubits by $1/f$ noise (2025), arXiv:2506.22394 [cond-mat.mes-hall].

[31] C. Knapp, M. Beverland, D. I. Pikulin, and T. Karzig, Modeling noise and error correction for Majorana-based quantum computing, Quantum **2**, 88 (2018).

[32] L. Mazza, M. Rizzi, M. D. Lukin, and J. I. Cirac, Robustness of quantum memories based on Majorana zero modes, Phys. Rev. B **88**, 205142 (2013).

[33] R. V. Mishmash, B. Bauer, F. von Oppen, and J. Alicea, Dephasing and leakage dynamics of noisy Majorana-based qubits: Topological versus Andreev, Phys. Rev. B **101**, 075404 (2020).

[34] F. Konschelle and F. Hassler, Effects of nonequilibrium noise on a quantum memory encoded in Majorana zero modes, Phys. Rev. B **88**, 075431 (2013).

[35] M. I. K. Munk, R. Egger, and K. Flensberg, Fidelity and visibility loss in Majorana qubits by entanglement with environmental modes, Phys. Rev. B **99**, 155419 (2019).

[36] A. R. Akhmerov, Topological quantum computation away from the ground state using Majorana fermions, Phys. Rev. B **82**, 020509(R) (2010).

[37] T. D. Stanescu and S. Das Sarma, Proximity-induced low-energy renormalization in hybrid semiconductor-superconductor Majorana structures, Phys. Rev. B **96**, 014510 (2017).

[38] H.-P. Breuer and F. Petruccione, *The Theory of Open Quantum Systems* (Oxford University Press, Oxford, 2002).

[39] B. D. Woods, T. D. Stanescu, and S. Das Sarma, Effective theory approach to the Schrödinger-Poisson problem in semiconductor Majorana devices, Phys. Rev. B **98**, 035428 (2018).

[40] S. Poncé, E. R. Margine, C. Verdi, and F. Giustino, EPW: Electron-phonon coupling, transport and superconducting properties using maximally localized Wannier functions, Comput. Phys. Commun. **209**, 116 (2016).

[41] I. Vurgaftman, J. R. Meyer, and L. R. Ram-Mohan, Band parameters for III-V compound semiconductors and their alloys, J. Appl. Phys. **89**, 5815 (2001).

[42] O. Madelung, *Semiconductors: Data Handbook*, 3rd ed. (Springer, Berlin, 2004).

SUPPLEMENTAL INFORMATION

Unless noted, values use the working-point wire, $T = 20$ mK, $L = 2$ μm, and $u = 0.1$ eV μm^{-3}. Excitation data use the initially empty Majorana level ($p = 0$). Excitation rates are per unit phonon occupation; efficiencies are in eV^{-1} μm^3. Semicolon-separated values follow the order of the listed conditions.

TABLE S1. Spectrum and excitation. PE denotes piezoelectric coupling.

Quantity	Condition	Value
Spectrum		
E_g; E_1	$E_1 - E_g \approx 13$ μeV	0.1260; 0.1394 meV
ϵ_M		0.746 μeV
k_F; π/k_F	Lower helical band	0.019 nm^{-1}; 167 nm
Majorana-density period		170 nm
ξ; L/ξ		355 nm; 5.6
Normal-state density; wavelength; velocity	k_F/π; $2\pi/k_F$; v_F	≈ 6 μm^{-1}; ≈ 330 nm; ≈ 70 km s^{-1}
Relative level error	$a = 2.5$ vs 1.25 nm; checked to 10 nm	$\leq 2 \times 10^{-4}$
Excitation kernel		
First pair: energy; rate	$E_1 + \epsilon_M$	0.1401 meV; 2.35×10^7 s^{-1}
First bulk-pair energy	$E_1 + E_2$	0.287 meV
Total rate	All excitation lines	2.72×10^8 s^{-1}
Rate fraction	0.14–0.30; > 0.5 meV	67%; 0.9%
Promotion vs pair-creation rates	Corresponding lines	-10% to $+26\%$
Fourier weight	$\lvert q_x \rvert \lesssim 0.04$ nm^{-1}; pair energies < 0.6 meV	90%
Phonon wave vector	0.14 meV: LA; TA	0.051; 0.090 nm^{-1}
Angular rate fraction	$\theta > 70°$; $> 60°$	87%; 95%
Transverse cutoff	$\hbar c_\nu / R$: LA; TA	0.14; 0.077 meV
Sound-speed; wave-vector ratios	$(c_L/c_T)^3$; $q_{\mathrm{TA}}/q_{\mathrm{LA}}$ (equal energy)	5.7; 1.8
Rate fraction by coupling	Deformation; LA PE; TA PE	77%; 15%; 8%
Pulse efficiency		
η, narrowband	$\Omega_c = 0.142$; 0.40 meV	0.44; 1.4×10^{-2}
	$\Omega_c = 0.50$; 1.0 meV	9.8×10^{-4}; 3.6×10^{-10}
	$\sigma = 5$ μeV, strongest line	> 1
η, broadband	94% of energy above 0.5 meV	1.95×10^{-3}
η, thermal	$T^* = 311$ mK	0.118
Field, chemical potential, and radius		
Gate-driven transition	$V_Z = 0.45$ meV	$\mu = 0.40$ meV
Excitation threshold	Away from transitions	0.08–0.16 meV; $\leq E_g + 0.06$ meV
Total rate	Field scan; gate scan	(1.6–3.7); (1.6–9.8)$\times 10^8$ s^{-1}
Kernel cutoff		≈ 0.8 meV
Gap minimum at $k = 0$	Field scan; gate scan	$V_Z < 0.338$ meV; $\mu > 0.234$ meV
Total rate	$R = 10$; 20; 40 nm	4.0×10^9; 2.7×10^8; 1.1×10^7 s^{-1}
Radius dependence	Total rate; first-line variation, $R =$ 10–40 nm	$\propto R^{-4.3}$; 13-fold
PE fraction at threshold	[111], [110]; [100]	0.58–0.60; 0.53
TA fraction of PE	[110]; other studied axes	$\approx 1/2$; majority
PE fraction $< 10\%$	Phonon energy	> 0.25–0.39 meV

TABLE S2. Parity, pulse strength, and escape. Energy-density and escape scans use broadband pulses spanning 0.1–0.6 and 0.1–1.0 meV, respectively.

Quantity	Condition	Value
Parity-projected equilibrium		
Majorana occupation ≈ 1	Odd wire parity	$T \lesssim 0.3$ K
ϵ_M/k_B		8.7 mK
Phonon energy density u (eV μm^{-3})		
$P_{\rm exc}/u$	$u \to 0$	1.50×10^{-2} eV^{-1} μm^3
Reduction of $P_{\rm exc}/u$	$u = 1$; 10; 100	0.7%; 7%; 48%
$\tau_{\rm return}$, initially empty level	$u = 0.001$–100	127.1–128.5 ns
$\tau_{\rm return}$, initially occupied level	$u = 0.001$–10	136.3–136.5 ns
Factorized residual $f_0/P_{\rm exc}$	$u \to 0$; $u = 100$	2.00; 0.64
Discarded weight	$k_{\max} = 4$, $u = 10$; 100	6×10^{-6}; 7×10^{-3}
Peak-leakage change	$k_{\max} = 4$ vs 2, $u = 10$	0.3%
Escape: residual flips per excitation		
Exact	Slow escape	$\Gamma_{\rm esc} \times 99$ ns
	$\Gamma_{\rm esc} = 10^4$; 10^7 s^{-1}	9.9×10^{-4}; 0.42
Half-saturation escape rate		$\approx 6 \times 10^6$ s^{-1}
Saturation value		0.642
Majorana-plus-bulk excitation fraction		0.641
Factorized	Slow escape	≈ 2
Factorized/exact	$\Gamma_{\rm esc} = 10^4$ s^{-1}	2×10^3

The reduction of $P_{\rm exc}/u$ follows saturation of $P_{\rm exc} = 1 - e^{-x}$. Escape is evaluated at the reference u.

TABLE S3. Seven pulse spectra: excitation, recovery, and coherence.

Excitation and recovery

Pulse	$P_{\mathrm{exc}}^{(0)}$	$P_{\mathrm{exc}}^{(1)}/P_{\mathrm{exc}}^{(0)}$	Bulk-pair share	Peak leakage $/P_{\mathrm{exc}}^{(0)}$	τ_{return} (ns) $p = 0,\ 1$
0.15 meV	4.2×10^{-2}	1.05	$< 10^{-4}$	0.52	122, 131
0.20 meV	1.9×10^{-2}	0.99	$< 10^{-4}$	0.54	130, 138
0.30 meV	5.8×10^{-3}	0.99	0.69	0.59	131, 139
0.50 meV	9.8×10^{-5}	1.01	0.94	0.70	129, 137
0.80 meV	4.8×10^{-9}	1.00	0.95	0.76	126, 134
Broadband	1.9×10^{-4}	1.00	0.36	0.59	128, 136
Thermal	1.2×10^{-2}	1.10	0.003	0.52	117, 125

Factorization error and coherence loss

Pulse	Factorized residual $f_0/P_{\mathrm{exc}}^{(0)}$	Peak leakage factorized/exact	$(1-\chi)/\bar{P}_{\mathrm{exc}}$	Bulk-pair paths via Majorana level
0.15 meV	1.86	0.98	1.00	–
0.20 meV	1.94	1.00	1.00	–
0.30 meV	1.98	1.69	0.75	0.64
0.50 meV	2.00	1.66	0.81	0.80
0.80 meV	2.00	1.65	0.82	0.82
Broadband	2.00	1.32	0.90	0.73
Thermal	1.96	0.99	1.00	–

Numerical checks

Quantity	Condition	Value
$P_{\mathrm{flip}}(10\ \mathrm{ms})$	All pulses; $p = 0, 1$	$< 4 \times 10^{-35}$
Discarded probability	All pulses; $p = 0, 1$; $k_{\max} = 2$	$\leq 3.6 \times 10^{-6}$
Peak leakage	0.20 meV	1.06×10^{-2}
Time of peak leakage	0.20 meV	176 ns
Time to $P_{\mathrm{leak}} < 10^{-6}$	0.20 meV	1.4 μs
Factorized $f_0(10\ \mathrm{ms})$	0.20 meV	3.76×10^{-2}

$p = 0, 1$ labels the initial Majorana occupation. Bulk-pair share: fraction of excitations creating two bulk quasiparticles. The last column gives the fraction of bulk-pair excursions involving the Majorana level. Residual occupations are evaluated at 10 ms; coherence losses are per wire.

TABLE S4. Coherence (Fig. 4). $D = 1 - |\chi|$ and $D_{\rm ref} = D(\epsilon_M = 1\ \mu{\rm eV})$. Ratios $D/D_{\rm ref}$ are evaluated well below the crossover. Losses are per wire unless noted.

Quantity	Condition	Value
Uniform wire		
Coherence loss	$\Omega_c = 0.20$ meV	$1.926 \times 10^{-2} = \bar{P}_{\rm exc}$
$\hbar/(2\epsilon_M)$	Working point	0.44 ns
Pair $(1, 2)$ decay rates	Capture (empty Majorana level); recombination (full); direct	$(3.0; 2.9; 2.4) \times 10^7$ s^{-1}
Final loss	$\Omega_c = 0.50$ meV	$0.81\bar{P}_{\rm exc}$
Time to within 1% of final loss	$\Omega_c = 0.50$ meV	250 ns
Time to leakage $< 1\%$ of peak	$\Omega_c = 0.50$ meV	≈ 780 ns
Two-wire loss	Independent events	$(1.5\text{–}2.0)\bar{P}_{\rm exc}$
Broadband loss	$\Gamma_{\rm esc} = 0$; 10^7 s^{-1}	$(1.76; 1.73) \times 10^{-4}$
κ_a	All retained modes	$< 4 \times 10^{-10}$
Relative change in $1 - \|\chi\|$	$\epsilon_M = 0.001$ neV–1 μeV	$< 3 \times 10^{-4}$
Gate gradient		
Lowest-mode centroid	$\delta U = 0.4$ meV	$0.68L$
κ_1	$\delta U = 0.2$; 0.4 meV	0.48; 0.89
Loss at $\epsilon_M = 1\ \mu$eV	$\Omega_c = 0.15$ meV, $\delta U = 0.4$ meV	6.6×10^{-2}
Crossover $\hbar\Gamma_1/2$	$\Omega_c = 0.15$ meV, $\delta U = 0.2$; 0.4 meV	9.0; 13.9 neV
All crossovers	Tested pulses and gradients	2–45 neV
$D/D_{\rm ref}$	$\Omega_c = 0.15$ meV, $\delta U = 0.4$; 0.2 meV	0.48; 0.86
$D/D_{\rm ref}$	$\Omega_c = 0.20$ meV, $\delta U = 0.4$; 0.2 meV	0.83; 0.92

TABLE S5. Hybrid-state normalization (Fig. 5). Rate ratios compare exact states with the effective model and bare vertex at $\gamma_t = \Delta_S$.

Quantity	Condition	Value
$\|Z_0 - Z(0)\|$		$\leq 1.2 \times 10^{-5}$
Excess of Z_a above $Z(0)$	Low-energy states	$\leq 2.3\%$
Z_a	$E_a/\Delta_S = 0.96$–0.97; $\gamma_t/\Delta_S = 0.5$; 1; 2	0.072; 0.038; 0.025
$H_{\rm eff}$ energy error	$E_a < 0.43\Delta_S$	$< 5\%$
22nd energy / Δ_S	Effective; exact	1.63; 0.97
Kernel ratio	Near threshold	1/4
Cumulative-rate ratio	$\Omega > 0.6\Delta_S$	0.22–0.27
$Z_0 Z_a$	Threshold to Δ_S	0.25 to 0.02
Rate ratio; $Z_0 Z_1$	First excitation	0.229; 0.251
Rate ratios	Higher states paired by index; last state	0.03–0.97; 2.9

TABLE S6. LO wire and matched Kitaev chains (Fig. 6). K_ℓ and K_h denote low- and high-density chains; triples follow $(K_\ell, K_h, \mathrm{LO})$. Ranges cover the seven reference pulses. Efficiency ratios are chain / wire.

Quantity	Condition	Value
Recovery and coherence		
P_{flip}	$t = 10$ ms, all models	$< 2 \times 10^{-34}$
τ_{return}	$(K_\ell, K_h, \mathrm{LO})$	97–105; 135–158; 117–131 ns
Factorized f_0/P_{exc}	$(K_\ell, K_h, \mathrm{LO})$	1.81–2.00; 1.90–2.00; 1.86–2.00
$(1-\chi)/\bar{P}_{\mathrm{exc}}$	$(K_\ell, K_h, \mathrm{LO})$	0.83–1.00; 0.70–1.00; 0.75–1.00
κ_a	All models	$< 4 \times 10^{-10}$
Excitation efficiency		
$\eta_{K_\ell}/\eta_{\mathrm{LO}}$	Narrowband < 0.5 meV; thermal; broadband	0.66–1.49; 1.34; 1.20
$\eta_{K_h}/\eta_{\mathrm{LO}}$	Narrowband < 0.5; 0.8; 1.0 meV	0.37–0.99; 7×10^2; 5×10^4
Change in η_{K_h}	$k_0 a = 1.0$ or 1.45; thermal, broadband	$< 1\%$
Change in η_{K_h}	Same $k_0 a$; narrowband ≤ 0.5; 1 meV	$< 11\%$; $< 35\%$
Momentum and boundaries		
Majorana-plus-bulk share	Coupling below 0.6 meV	$\approx 2/3$
$\lvert k_a \pm k_0 \rvert$; Fourier tail	LO wire	< 0.05 nm^{-1}; q_x^{-6} or steeper
$k_a + k_0$; Fourier tail	K_h	≈ 1 nm^{-1}; q_x^{-2}
Fourier-tail reduction	100-nm edge window on transition densities; $\lvert q_x \rvert = 0.1$–0.5 nm^{-1}	10^2–10^6
Bulk-pair share	K_h, near 1 meV	$\approx 1/2$
Coupling from $\theta < 30^\circ$	$\Omega = 0.6$–1.2 meV; K_h; LO	95%; 0.4%
Coupling from $\theta > 70^\circ$	$\Omega < 0.6$ meV, all models	79%–95%
Efficiency drop to 1 meV	From threshold; low; high density	10^9; 10^4
Field and chemical-potential scans		
Gap minimum near k_F	Field scan ($\mu = 0$); gate scan	$V_Z > 0.338$ meV; $\mu < 0.234$ meV
Deviation of η_{K_ℓ}	In this region; thermal; broadband	$\leq 38\%$; $\leq 47\%$
Narrowband deviation	Same region, 0.15, 0.20, 0.40 meV	Largest factor 2.2; mean excess 25%
Thermal η_{LO}	$\mu = 0.20$; -0.30 meV	0.048; 5.3
$\hbar v_F$	$V_Z = 0.225$ meV; K_ℓ; LO k_F; LO $k = 0$	4.8; 34; ≈ 20 meV nm
Modes below the k_F minimum	$V_Z = 0.225$ meV; K_ℓ; LO	21; 6
Thermal $\eta_{K_\ell}/\eta_{\mathrm{LO}}$	$V_Z = 0.225$ meV; $\mu = 0.375$ meV	1800; 23
Selection rule		
$\langle \sigma_x \tau_x \rangle$	Majorana spinors, $V_Z = 0.225$ meV	-0.89
Weak-line suppression (median)	$V_Z = 0.225$–0.25 meV; versus k_F lines within 0.1 meV above the minimum	7–10 fold
Weak-line suppression (median)	Same range; versus K_ℓ lines	18–28 fold
Thermal η_{LO}	Working point to $V_Z = 0.225$ meV	0.11–0.20
Weak-line share	$V_Z = 0.225$ meV	60%
E_g; fraction of reference gap	$V_Z = 0.225$ or $\mu = 0.375$ meV	25 μeV; 1/5
Low-energy rates $\geq k_F$-branch rates	Chemical-potential scan	$\mu \geq 0.35$ meV
Thermal η_{LO}; enhancement	$\mu = 0.375$ meV	3.7; 31

Weak lines lie below the k_F-branch minimum. Efficiencies are in eV^{-1} μm^3.